

## Article

# Petrology and Age of the Yamaat Uul Mafic Complex, Khangai Mountains, Western Mongolia

Roman Shelepaev<sup>1,2</sup>, Maria Shapovalova<sup>1,\*</sup>, Vera Egorova<sup>1,2</sup>, Yaroslav Shelepov<sup>1,2</sup>,  
Tumen-Ulzii Oyunchimeg<sup>3</sup> and Nadezhda Tolstykh<sup>1</sup>

<sup>1</sup> Sobolev Institute of Geology and Mineralogy, Siberian Branch of the Russian Academy of Sciences, Novosibirsk 630090, Russia; rshel@igm.nsc.ru (R.S.); verae@igm.nsc.ru (V.E.); shelepov@igm.nsc.ru (Y.S.); tolst@igm.nsc.ru (N.T.)

<sup>2</sup> Department of Geology and Geophysics, Novosibirsk State University, Novosibirsk 630090, Russia

<sup>3</sup> Institute of Geology, Mongolian Academy of Sciences, Labor Union St., Ulaanbaatar 13330, Mongolia; oyuna22@yahoo.com

\* Correspondence: shapovalovam@igm.nsc.ru

**Abstract:** The Yamaat Uul mafic complex with Cu-Ni mineralization is located in the Khangai Mountains of Western Mongolia. We have received new unique data for mafic rocks of the complex: U-Pb dating (SHRIMP II), mineralogy (WDS) and geochemistry (XRF, ICP-MS), Sm-Nd and Rb-Sr isotope data and sulphur isotopes. The Yamaat Uul mafic complex consists of two intrusions: Intrusion 1 is represented by rocks of plagioclase cumulates and olivine–pyroxene cumulates; Intrusion 2 consists of monzogabbro. Intrusions 1 and 2 are different in composition of minerals such as olivine, plagioclase and biotite. The monzogabbro has higher contents of incompatible elements (REE, K, Ti, P) than rocks of Intrusion 1. Zircon U-Pb dating of the anorthosite and Bt-Am-Ol gabbro-norite shows a Late Permian age ( $255.8 \pm 2.9$  Ma and  $262.6 \pm 3.1$  Ma, respectively) for the Yamaat Uul mafic complex. All of the rocks of the complex are derived from a unified parental melt due to different amounts of trapped melts in plagioclase and olivine–pyroxene cumulates and without crustal contamination. The Cu-Ni mineralization of the complex has a low degree of evolution of the sulphide melt, similar to PGE-Cu-Ni mafic–ultramafic intrusions of the Khangai Mountains (Nomgon and Oortsog Uul). The Yamaat Uul mafic complex together with other mafic–ultramafic intrusions of the Khangai Mountains is related to the Khangai LIP and can be considered as potential for the PGE-Cu-Ni. The new geological, petrological, geochemical and isotope–geochronological data can later be used to reconstruct the geotectonics of the Khangai Mountains and the Central Asian orogenic belt as a whole.

**Keywords:** Khangai Mountains; Permian; mineralogy; petrology; geochemistry; Sr-Nd isotope; sulphur; Cu-Ni mineralization; LIP



**Citation:** Shelepaev, R.; Shapovalova, M.; Egorova, V.; Shelepov, Y.; Oyunchimeg, T.-U.; Tolstykh, N. Petrology and Age of the Yamaat Uul Mafic Complex, Khangai Mountains, Western Mongolia. *Minerals* **2023**, *13*, 833. <https://doi.org/10.3390/min13060833>

Academic Editors: Richard E. Ernst and Hafida El Bilali

Received: 14 May 2023

Revised: 6 June 2023

Accepted: 15 June 2023

Published: 20 June 2023



**Copyright:** © 2023 by the authors. Licensee MDPI, Basel, Switzerland. This article is an open access article distributed under the terms and conditions of the Creative Commons Attribution (CC BY) license (<https://creativecommons.org/licenses/by/4.0/>).

## 1. Introduction

Mafic–ultramafic rocks derived from picritic and basaltic magmas are widespread in the orogenic belts of Central and Southeast Asia and are related to large igneous provinces (LIPs) [1]. Recent study of mafic–ultramafic layered intrusions with sulphide mineralization has been undertaken in south-eastern Siberia [2–5], Vietnam [6–9], China [10–14] and Mongolia [15–17]. Such intrusions are derived from mantle magmas and their study contributes significantly to petrological models and reconstruction of the evolutionary history of geological structures.

Such intrusions are also of great interest in the search for associated Cu-Ni-PGE mineralization. Permian large igneous provinces (LIPs) include the Emeishan and Tarim LIPs [4,18–20] and Siberian Traps [1,21].

Early studies of Khangai batholith metallogeny show the role of the mantle plume in the formation of the Late Palaeozoic magmatism of Central Asia, including Mongolia [22]. All granitoid and ultramafic–mafic complexes of the Khangai Mountains can

be considered as fragments of the plutonic part of a large igneous province [23], which has been proposed as the Permian Khangai LIP [24]. Granitoids of the Khangai batholith have been studied in detail—divided by age [25,26] and by geochemical and isotopic characteristics [27–29]. Little information has been accumulated about the mafic–ultramafic intrusions in the Khangai region, but some of the Permian intrusions have already been identified (Figure 1) [15,17,30].

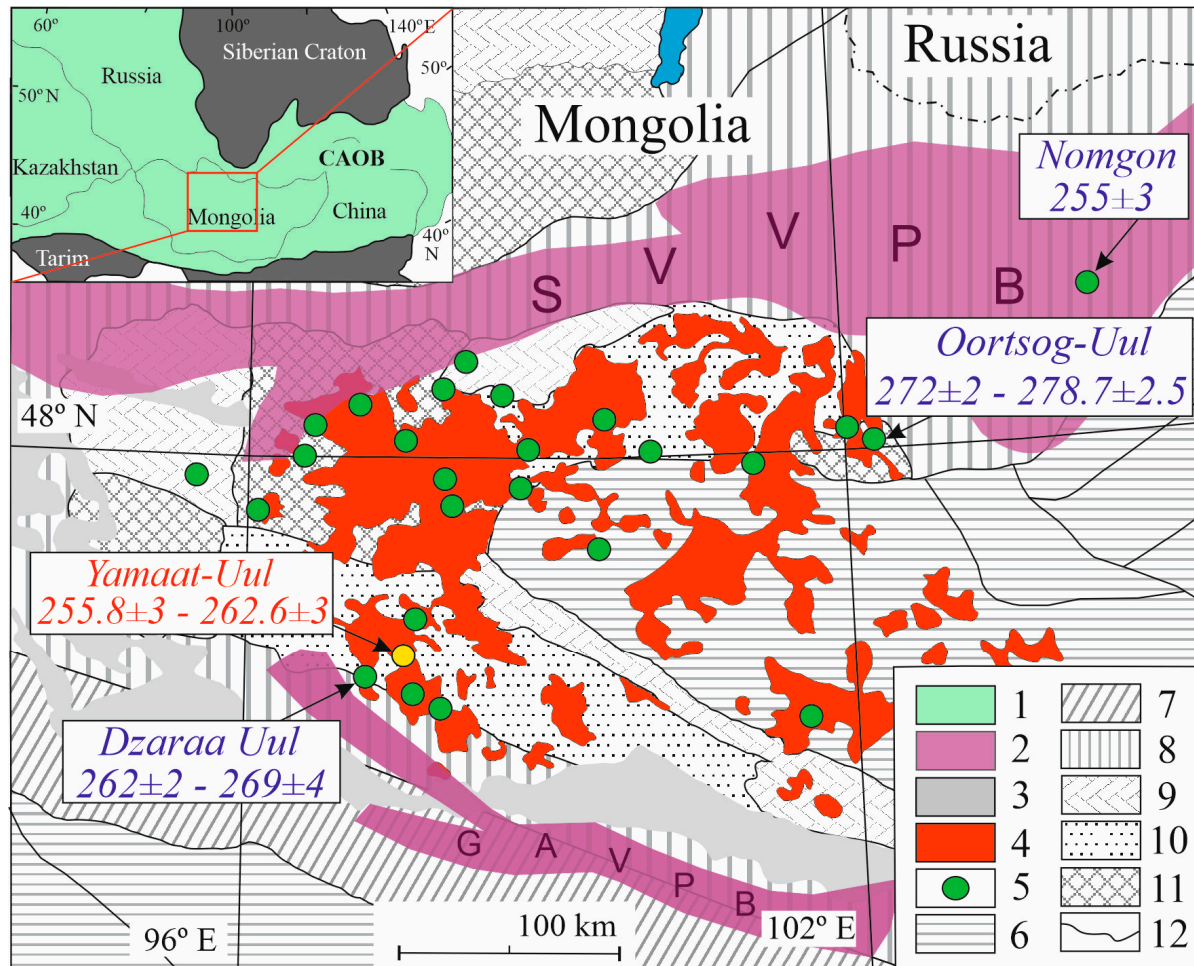


**Figure 1.** A geologic map of the mafic–ultramafic intrusions location within Khangai batholith (modified after [31,32]). 1—Central Asian orogenic belt (CAOB); 2—volcano–plutonic belt (SVVPB—Selenga–Vitim volcano–plutonic belt, GAVPB—Gobi–Altay volcano–plutonic belt); 3—Mesozoic–Cenozoic troughs; 4—Late Palaeozoic granitoids of the Khangai batholith; 5—Permian gabbros of the Khangai Mountains; 6–9—orogens: 6—Middle–Late Palaeozoic (Hercynides), 7—Early–Middle Palaeozoic (late Caledonides), 8—Vend–Early Palaeozoic (early Caledonides), 9—Neoproterozoic; 10—tectonic blocks with the Early Precambrian basement; 11—tectonic blocks with the Pre-Vend orogenic basement; 12—main tectonic boundaries. Red box—study area.

In this paper, we present new zircon U–Pb ages, Sm–Nd, Rb–Sr isotope data and detailed petrographic, mineralogical and geochemical study of the large Yamaat Uul mafic complex in the Khangai region. The purpose of this research was to identify the typomorphic mineralogical and geochemical features of the Yamaat Uul mafic complex, define the differentiation process of the parental magma and to better understand the tectonic setting of this region during the Permian. In addition, we will consider the sulphide mineralization in the Yamaat Uul complex and the sulphur isotopic composition in comparison with similar Permian intrusions and discuss its PGE–Cu–Ni potential.

## 2. Geological Setting and Geological Occurrence

The Yamaat Uul mafic complex is located in the Khangai Mountains of Western Mongolia and is part of the CAOB (Figure 1). The Khangai Mountains (Figure 1) are represented by the Khangai batholith, which is bounded by the Selenga–Vitim volcano–plutonic belt in the north and the Gobi–Altay volcano–plutonic belt in the south [33]. Together with other mafic–ultramafic intrusions, they are an early phase of the Khangai batholith [15] according to one of the theories of the Khangai LIP [24].

The CAOB is the largest juvenile Phanerozoic orogenic belt in the world and has developed over about 800 Ma. It is located between the East European, Siberian, North China and Tarim cratons and covers a large area of Russia from the Urals through Altai–Sayan and Transbaikalia to the Sea of Okhotsk, as well as areas of Kazakhstan, Kyrgyzstan, Uzbekistan, Mongolia, Northwest China and Northeast China [34]. The CAOB is composed of fragments of Precambrian continental blocks and Palaeozoic island arcs, ophiolites and volcanic rock assemblages formed by the action of various geodynamic processes [34–38]. The Yamaat Uul complex is located in the southern branch of the Khangai. Structurally and tectonically, it is located in the Baidrig terrane of the Dzavhan–Orkhon block [39], which in turn is part of the Central Mongolian terrane [40,41].

The Yamaat Uul mafic complex is the largest layered intrusion in Western Mongolia with the Cu–Ni mineralization. It is located on the left bank of the Dzavhan River, 25 km from Guulin Som of the Gobi–Altai aimag and 100 km from Altai City. The complex consists of outcrops of several large bodies, 20 × 20 km, which extend from north–west to south–east (Figure 2). The entire complex can be conventionally divided into three parts: Northwestern, Central and Southeastern. The geological map of Mongolia [L-47-VIII] shows only the Central part of the Yamaat Uul complex, but we found outcrops in other parts of the complex during field trips in 2014–2017.

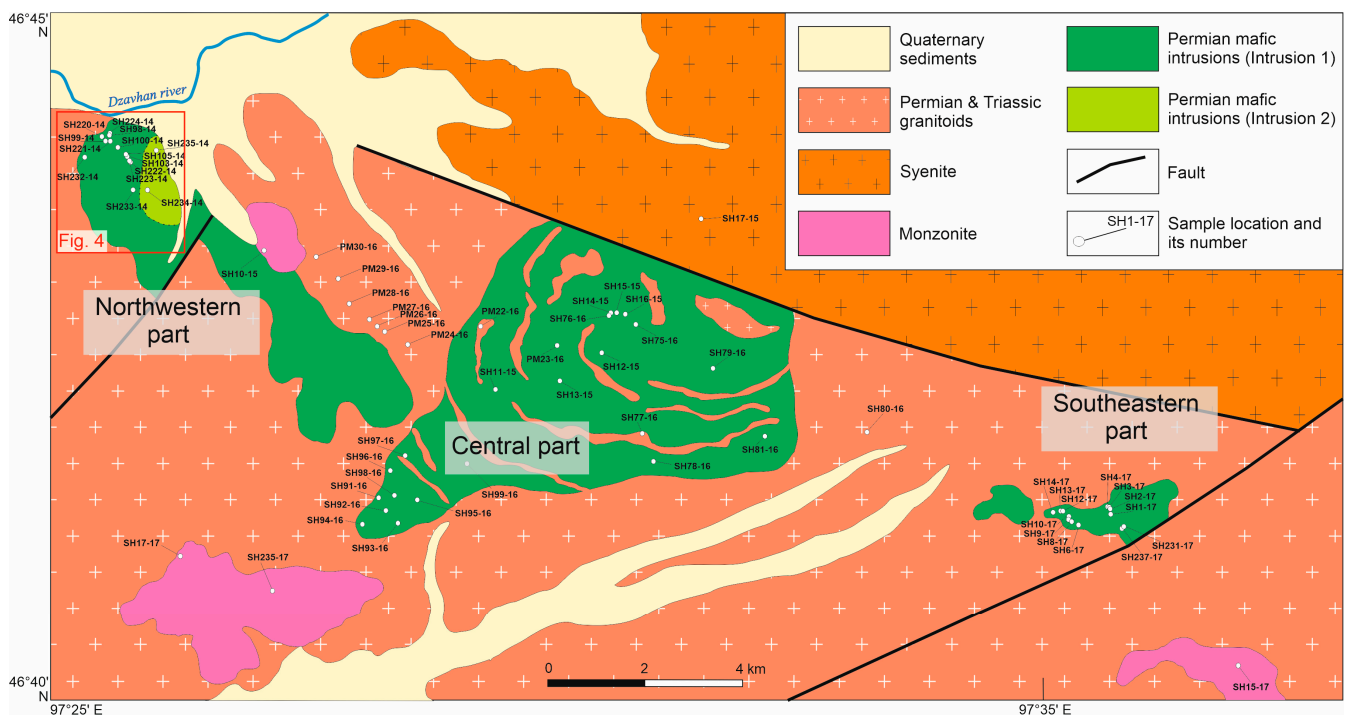


**Figure 2.** Simplified geological map of the Yamaat Uul mafic complex showing the distribution of lithological unites and sample's location.

The most important part for the reconstruction of the genesis is the Northwestern part of the complex, where we can observe the rock outcrops from two intrusions. Intrusion 1 is mainly represented by two groups of rocks:

- (1) leucogabbro and anorthosite (plagioclase cumulate) (Figure 3a–c) and clearly marked in blue on the magnetic anomalies map (Figure 4a);
- (2) biotite–amphibole (Bt-Am) gabbro and olivine (Ol) gabbronorite (olivine–pyroxene cumulates), located south of the previous (Figure 3d) and highlighted in yellow and green on the magnetic anomalies map (Figure 4a).

Intrusion 2 is composed of monzogabbro and occurs only in the Northwestern part of the complex; the samples SH234-14 and SH235-14 are involved (Figure 3e), which are marked by a red spot in the Eastern part on the magnetic anomalies map (Figure 4 b,c).

The Southeastern part is characterized by rocks of two groups of Intrusion 1: leucogabbro and gabbro and gabbronorite (without forming separate clusters). The gabbro is characterized by rhythmic layering (Figure 3f,g).

The Central part of the Yamaat Uul complex is composed of leucogabbro, gabbro and gabbronorite. The gabbro is characterized by rhythmic layering (Figure 3f,g); the Central part is a series of rhythmically layered rocks from Bt-Am-Ol gabbronorite to Bt-Am gabbro (Table 1). The layered structure of the mafic complex is clearly visible on the satellite image and in the photos (Figure 3m,n). The thickness of the layers varies from 5 to 20 m. The rocks of the Northwestern and Southeastern parts have subvertical bedding, whereas the Central part lies subhorizontal. Thus, the Yamaat Uul mafic complex is lopolith in plan, as are the major layered intrusions such as the Bushveld in South Africa and Sudbury in Canada [42,43].

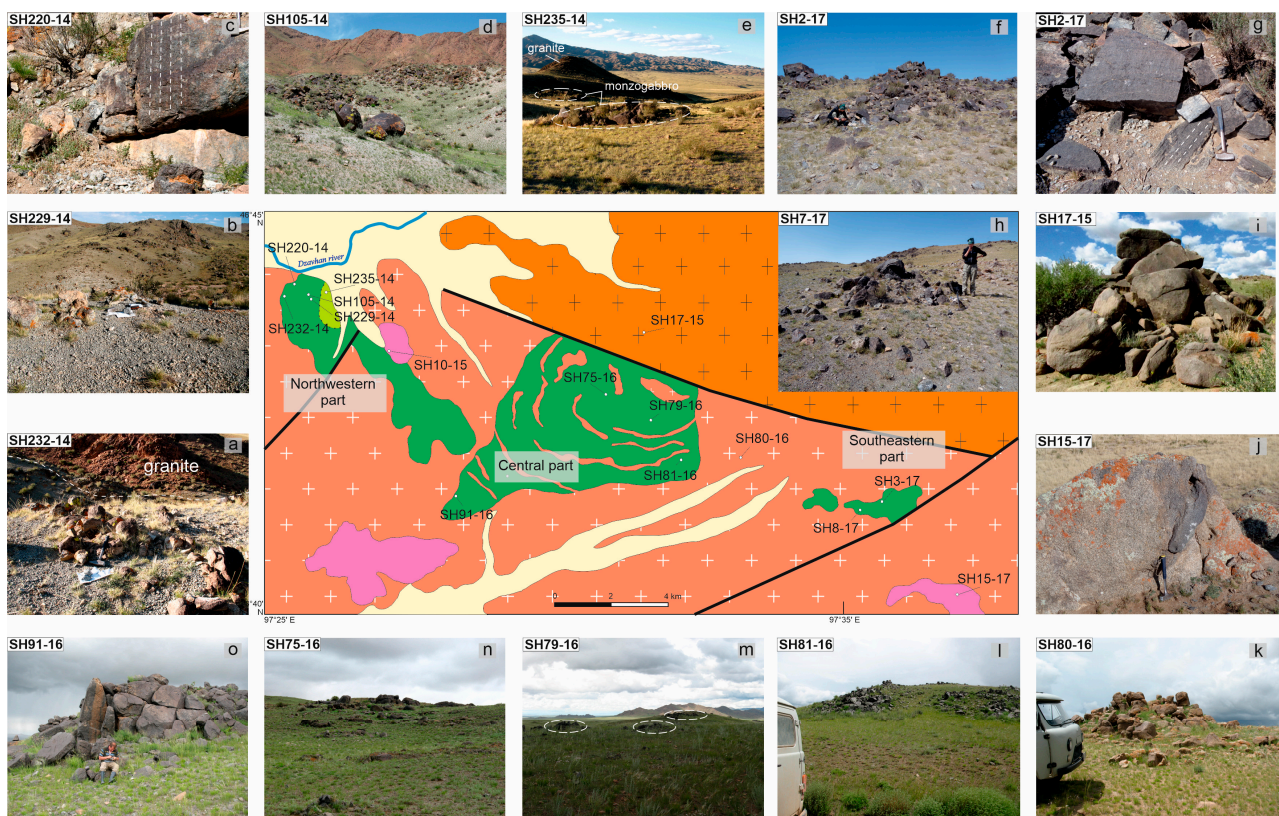


**Figure 3.** Photos of outcrops of the Yamaa-Uul mafic complex. (a–c) Plagioclase cumulates of Northwestern part; (d) pyroxene cumulates of Northwestern part; (e) monzogabbro of Intrusion 2; (f–h) Bt-Am leucogabbro of Southeastern part; (i) quartz syenite; (j) quartz monzodiorite; (k) Bt monzogranite; (l–o) gabbroids of Central part. Leucogabbro with fine subvertical layering (c,g). Names of rocks are in Table 1.

**Table 1.** Description of representative rock samples from Yamaat Uul mafic complex and surrounding rocks.

	Sample No.	Part of the Complex	Name of Rock	Latitude (N)	Longitude (E)
<b>Intrusion 1</b>					
1	SH100-14	Northwestern	Bt-Am-Ol gabbronorite	46.728381	97.447151
2	SH102-14	Northwestern	Bt-Am-Ol gabbronorite	46.727738	97.447997
3	SH103-14	Northwestern	Bt-Am-Ol gabbronorite	46.727333	97.448625
4	SH105-14	Northwestern	Bt-Am-Ol gabbronorite	46.726724	97.449163
5	SH220-14/2	Northwestern	Anorthosite	46.729082	97.445146
6	SH220-14/10	Northwestern	Leucogabbro	46.729274	97.444686
7	SH225-14	Northwestern	Leucogabbro	46.729533	97.444943
8	SH227-14	Northwestern	Anorthosite	46.729367	97.444792
9	SH228-14	Northwestern	Am gabbro	46.729347	97.444766
10	SH229-14	Northwestern	Bt leucogabbro	46.729296	97.444747
11	SH11-15	Central	Bt-Am-Ol melagabbronorite	46.70177	97.50741
12	SH12-15	Central	Bt-Am-Ol melagabbronorite	46.7058	97.52436
13	SH15-15	Central	Bt-Am gabbro	46.71023	97.52673
14	SH16-15/1	Central	Bt-Am gabbro	46.71004	97.5284
15	SH79-16	Central	Bt-Am gabbro	46.70414	97.54219
16	SH81-16	Central	Bt-Am gabbro	46.69661	97.55044
17	SH94-16/6	Central	Bt-Am gabbronorite	46.68693	97.48623
18	SH97-16	Central	Bt-Am-Ol gabbronorite	46.69443	97.49313
19	SH98-16/1	Central	Bt-Am-Ol gabbro	46.68999	97.49137
20	SH235-17	Central	Bt-Am gabbro	46.679603	97.471888
21	SH2-17	Southeastern	Bt-Am leucogabbro	46.688659	97.605492
22	SH5-17	Southeastern	Bt-Am leucogabbro	46.687670	97.602768
23	SH7-17	Southeastern	Bt-Am leucogabbro	46.687253	97.599314
24	SH14-17	Southeastern	Bt-Am leucogabbro	46.688338	97.596355
25	SH231-17	Southeastern	Bt-Am-Ol gabbronorite	46.686665	97.607608
26	SH232-17	Southeastern	Bt-Am gabbro	46.686665	97.607608
<b>Intrusion 2</b>					
27	SH234-14	Northwestern	Bt-Am-Ol monzogabbro	46.723678	97.451858
28	SH235-14	Northwestern	Bt-Am-Ol monzogabbro	46.728046	97.453226
<b>Felsic and intermediate rocks</b>					
29	SH10-15		Q monzodiorite	46.71689	97.47012
30	SH16-17		Q monzodiorite	46.671505	97.625913
31	SH17-17		Q monzonite	46.683439	97.456712
32	PM30-16		granodiorite	46.716230	97.478799
33	SH80-16		Bt monzonite	46.6971	97.5668
34	SH17-15		Bt-Cpx-Am syenite	46.72047	97.54023

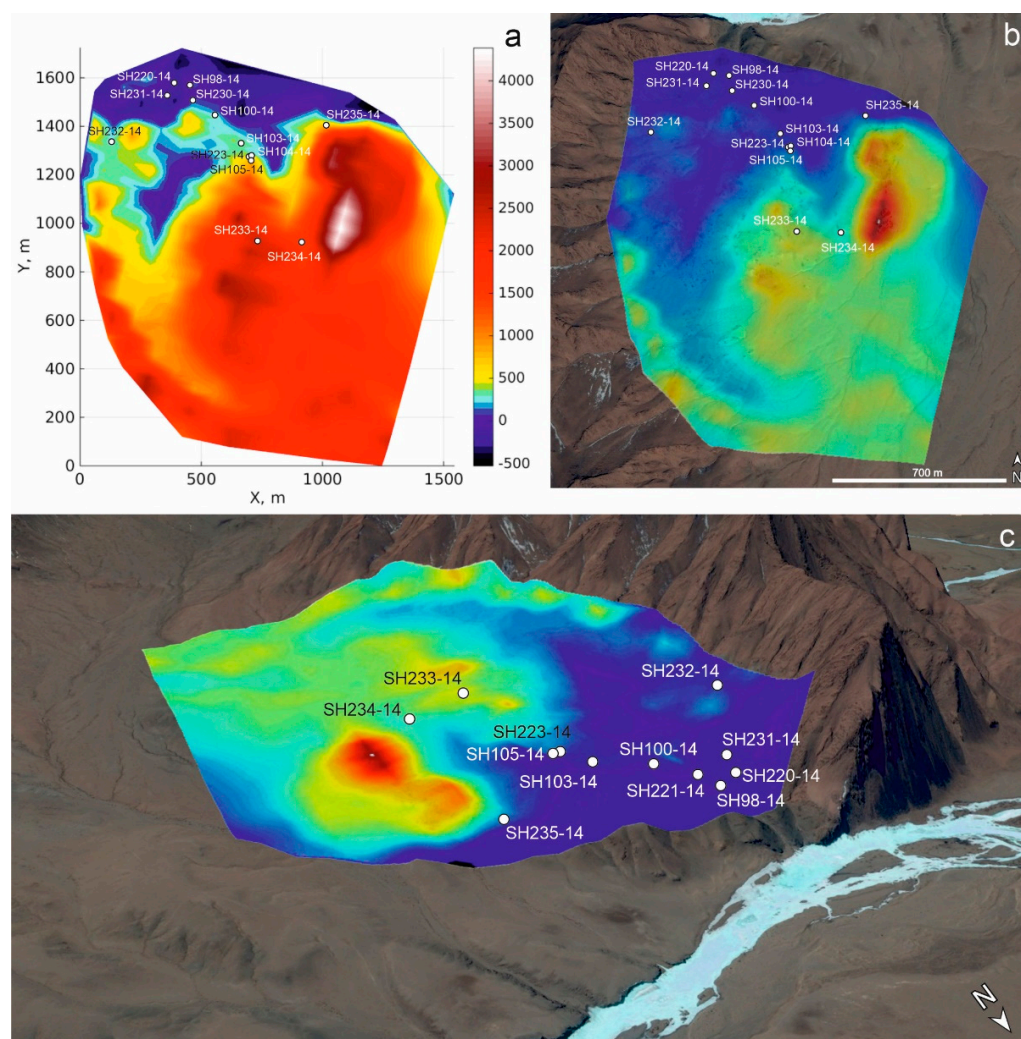


**Figure 4.** (a) Magnetic anomalies map and sample's location of the Northwestern part of the Yamaat Uul mafic complex; (b,c) shaded-relief magnetic anomaly map of the Northwestern part of the Yamaat Uul mafic complex: view from above (b), view from the northeast (c).

The boundaries of the Yamaat Uul mafic complex are mostly obscured by Quaternary sediments; outcrops of single round stones are mostly observed (Figure 3a–k). The complex's rocks have intrusive contact with later Permo-Triassic granites in the Northwestern part (Figure 3a); gabbro of the Central part is intensely intruded by granite dikes (Figure 2). There are outcrops of syenite (Figure 3h) to the north of the Central part—the contact with which is also sodded. Outcrops of monzonite and monzodiorite (Figure 3j), probably of a later age than the rocks of the mafic complex, are found in various parts of the complex. In general, the Yamaat Uul complex is surrounded by granitoids of the Khangai batholith [29] (Figure 3k).

The Yamaat Uul mafic complex contains sulphides, which are represented by disseminated and schlieren (droplets, globules) types. The Central part of the complex is characterized by sulphide disseminations only, while in other parts, both sulphide dissemination and sulphide schlieren are found. The sulphide mineralization represented by the chalcopyrite–pentlandite–pyrrhotite composition has been previously described [32].

### 3. Sampling and Analytical Methods

A collection of about 100 samples of mafic rocks was gathered by authors during the 2014–2017 field works on the Khangai region in Mongolia. Twenty-eight mafic samples of all parts of the Yamaat Uul complex were selected for this study (Table 1). Big-volume

samples of two rock types (SH105-14, SH220-14) were taken for zircon separation and U-Pb dating. Based on petrography, less altered samples were chosen for crushing and grinding to powder for whole-rock analyses. Ten samples were chosen for isotope analyses of Sm-Nd, Rb-Sr and S—systems. Most analyses were carried out in the Analytical Center for multi-elemental and isotope research of the Sobolev Institute of Geology and Mineralogy, Siberian Branch of the Russian Academy of Sciences (IGM SB RAS) in Novosibirsk, Russia.

### 3.1. Petrography

The Yamaat Uul mafic complex consists of two intrusions. Intrusion 1 is represented by plagioclase cumulates and olivine–pyroxene cumulates. Intrusion 2 consists of monzogabbro, which occurs only in the Northwestern part of the complex. Plagioclase cumulates (Figure 5a,b) are represented by leucogabbro and anorthosite with plagioclase contents of 80–95 vol%, and the interstitials contain anhedral grains of clinopyroxene, amphibole and very rarely biotite. Plagioclase is almost always zoned. Ore mineralization is represented by rare disseminations of chalcopyrite, pyrrhotite, magnetite and pyrite. The structure of the rocks is ophitic, subophitic and poikilophitic. The secondary minerals of chlorite, epidote, actinolite and rutile are common.

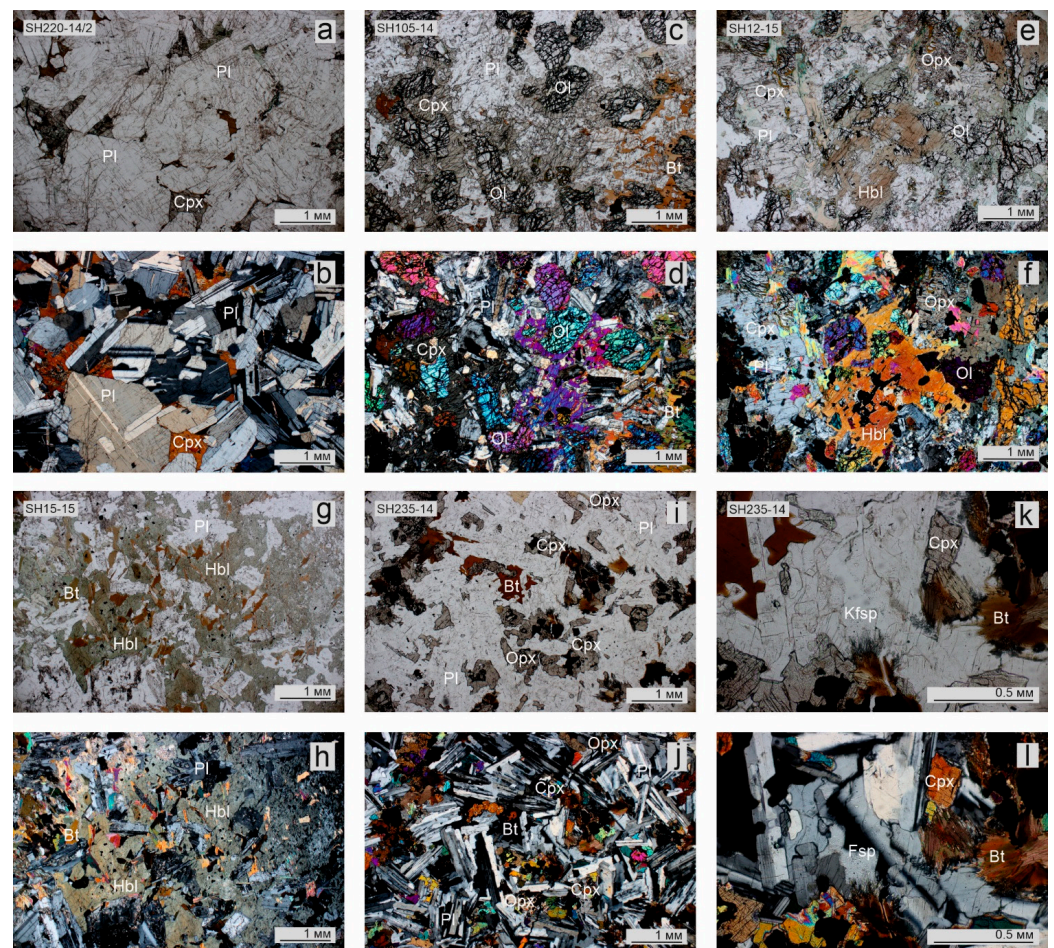


**Figure 5.** Photos of thin sections of the Yamaat Uul mafic complex: (a,b) plagioclase cumulate of Intrusion 1; (c–h) pyroxene cumulate of Intrusion 1: (c,d) olivine gabbro, (e,f) Am melagabbronorite, (g,h) Am gabbro; (i–l) monzogabbro of Intrusion 2. (a,c,e,g,i,k)—PPL; (b,d,f,h,g,l)—XPL. Ol—olivine, Cpx—monoclinic pyroxene, Opx—rhombic pyroxene, Hbl—hornblende, Bt—biotite, Pl—plagioclase, Fsp—K-Na feldspar.

Olivine–pyroxene cumulates (Figure 5c–h) are represented by amphibole melagabbronorite (Figure 5e,f), amphibole gabbro (Figure 5g,h), olivine gabbro (Figure 5c,d) and

olivine gabbronorite, in which the basic plagioclase content varies from the first percent (in melanocratic varieties) to 50 vol%. Olivine forms relatively large crystals, often surrounded by clinopyroxene (Figure 5c,d), amphibole in gabbroids or only amphibole in hornblende melagabbronorite (Figure 5e,f). The oikocryst of poikilitic clinopyroxene in gabbroids contains zonal distributed chadacrysts of plagioclase, indicating concomitant growth of plagioclase and clinopyroxene. In contrast to plagioclase cumulates, the amount of biotite increases in pyroxene cumulates. Its content is higher in melanocratic rocks than in mesocratic ones. The ore mineralisation is represented by disseminated, drop-shaped or schliere sulphide grains (cubanite, chalcopyrite, pyrrhotite, pentlandite) and schliere titanomagnetite ores. The structure of the rocks is ophitic, subophitic and poikilophitic. The secondary minerals of saussurite, chlorite, actinolite and iddingsite are locally distributed.

Monzogabbro of Intrusion 2 (Figure 5i,j) is leucocratic rocks consisting of plagioclase (60 vol%), olivine (10 vol%), clinopyroxene (5 vol%) and orthopyroxene (5 vol%), amphibole (5 vol%), biotite (10 vol%) and K-Na feldspar (5 vol%). Olivine and plagioclase are euhedral; clinopyroxene and biotite are anhedral. Orthopyroxene forms rims around olivine, and amphibole usually forms rims around clinopyroxene. Feldspar is located between euhedral plagioclase grains (Figure 5k,l). The structure of the rocks is ophitic, gabbro-ophytic and crowned. Monzogabbro contains disseminated oxide mineralization: magnetite and ilmenite.

### 3.2. Mineral Chemistry

The mineral composition of the Yamaat Uul mafic complex was determined in 24 thin sections previously prepared and polished at the laboratory of the IGM SB RAS. In total, 600 mineral chemistry analyses were conducted with wavelength-dispersive spectroscopy (WDS) in the Analytical Center of multi-elemental and isotope research of SB RAS under a JEOL JXA-8230 electron microprobe with five WDS detectors with LDE, TAP, PET-J, PET-H and LIF-L crystals. The analyses were determined with a current of 20 kV and 30 nA (100 nA for olivine) and 3 µm beam aperture. The analysis time ranged from 20 to 60 s per element, according to the expected abundance.

### 3.3. Zircon Separation and Analysis

Zircon separation was conducted in the IGM SB RAS with a standard procedure of crushing, panning, heavy-liquid and magnetic separation techniques. Zircon grains were handpicked under a binocular and then mounted in a 6 mm epoxy resin disc. All grains were half-polished to observe the internal structure using cathodoluminescence (CL) and transmitted light. The CL imaging was conducted at the Centre of Isotopic Research of the Russian Geological Research Institute (VSEGEI) using the scanning electron microscope MX2500 S (CamScan, Great Britain, Cambridge) and operated at an accelerating voltage of 12 kV and working distance of 30 mm. The locations for the spot analysis on zircon grains were selected using CL images (Figure 6a,b) and photomicrographs (transmitted light) to avoid mineral inclusions and cracks. Zircons from the samples SH220-14/2 and SH105-14 were analysed for U–Pb ages at the VSEGEI, Russia, with a SHRIMP II, following the standard procedures described in [44]. Prior to each analysis, the rastering of primary beams was applied to minimize contamination by surface Pb. U–Pb ages and concordia diagrams were calculated and plotted using IsoplotR software (ver. 3.75; [45]), respectively; the concordia age of each sample incorporates errors on decay constants and includes evaluation of the concordance of apparent ages. The concordia ages and errors are presented at the two-sigma level. All analyses of zircons are given in Table 2.

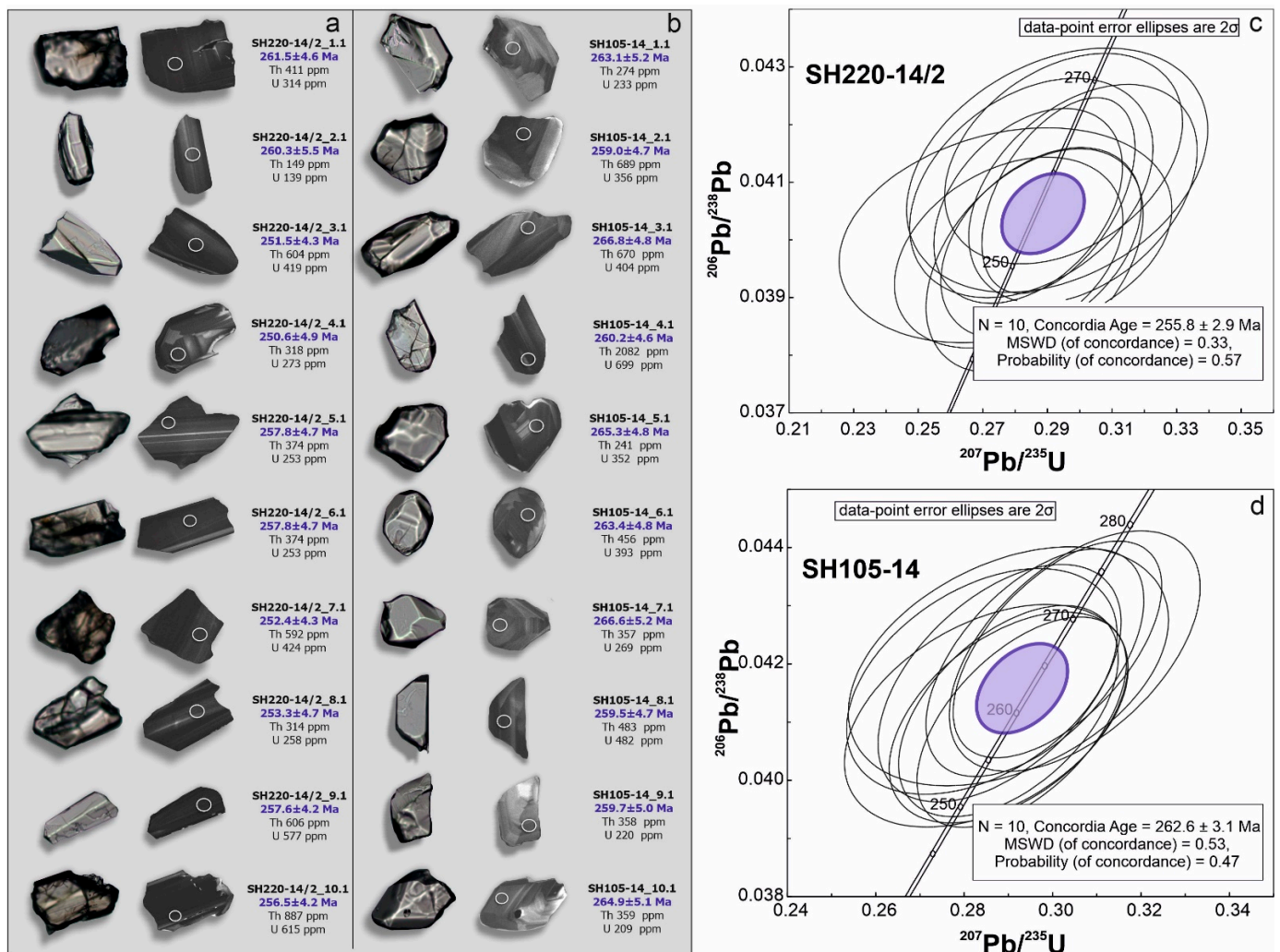


**Figure 6.** Transmitted light and CL images, U-Pb spot locations and ages for zircons from anorthosite (sample SH220-14/2) (a) and Bt-Am-Ol gabbro (SH105-14) (b). Concordia diagram for zircons from anorthosite (sample SH220-14/2) (c) and Bt-Am-Ol gabbro (SH105-14) (d).

### 3.4. Whole-Rock Major and Trace Elements

Whole-rock major element oxides were determined with XRF using an ARL 9900 (Thermo Scientific, Basel, Switzerland) according to the method in [46]. Trace elements were analysed with inductively coupled plasma emission-mass spectroscopy (ICP-MS) using an Element-1 MAT (Finnigan, Germany) according to the method in [47]. The element abundances and ratios were normalized to chondritic CI and primitive mantle (PM) values, with reference to [48,49], respectively. Representative analyses of major and trace element contents (in wt.% and ppm, respectively) are given in Table 3.

### 3.5. Whole-Rock Sm-Nd, Rb-Sr and S Isotopic Analyses

Nd isotope compositions were determined at the Institute of Geology and Geochemistry of the Ural Division of the Russian Academy of Sciences in Yekaterinburg. Prepared samples were decomposed with 3%  $\text{CH}_3\text{COOH}$  in a Teflon beaker at room temperature. Neodymium was separated during two stages: in the first stage, total REE was isolated with stepwise elution on cationite AG-50  $\times$  8 (200–400 mesh), and then with extraction chromatography on columns filled with KEL-F powder coated with ionite (HDEHP). The isotopic composition was measured on a Finnigan MAT-262 multicollector solid-phase mass spectrometer in the static regime. The measured  $^{143}\text{Nd}/^{144}\text{Nd}$  ratios were normalized to  $^{146}\text{Nd}/^{144}\text{Nd} = 0.7219$ . External uncertainty and reproducibility were controlled using

systematic measurements of the JNdi-1 = 0.512115 [50] international standards. The blank contamination for Nd was as low as 90 pg.

**Table 2.** Isotope parameters and ages of zircons from rocks of the Yamaat Uul mafic complex.

Spot	U ppm	Th ppm	$\frac{^{232}\text{Th}}{^{238}\text{U}}$	$^{206}\text{Pb}_t$ %	$^{206}\text{Pb}^*$ ppm	Isotope Parameters						Rho	Age, Ma			
						$\frac{^{207}\text{Pb}^*}{^{206}\text{Pb}^*}$	±%	$\frac{^{207}\text{Pb}^*}{^{235}\text{U}}$	±%	$\frac{^{206}\text{Pb}^*}{^{238}\text{U}}$	±%		$\frac{^{206}\text{Pb}}{^{238}\text{U}}$	$\frac{^{207}\text{Pb}}{^{206}\text{Pb}}$		
Anorthosite (SH220-14/2)																
1.1	314	411	1.35	0.28	11.20	0.0518	4.8	0.295	5.1	0.04141	1.8	0.352	261.5	±4.6	274	±110
2.1	139	149	1.11	0.00	4.92	0.0516	6.1	0.293	6.5	0.04121	2.1	0.330	260.3	±5.5	269	±140
3.1	419	604	1.49	0.35	14.40	0.0507	4.9	0.278	5.2	0.03978	1.7	0.337	251.5	±4.3	226	±110
4.1	273	318	1.20	0.00	9.28	0.0523	4.3	0.286	4.8	0.03964	2.0	0.419	250.6	±4.9	300	±99
5.1	211	264	1.29	0.00	7.42	0.0506	5.0	0.285	5.4	0.0409	1.9	0.360	258.4	±4.9	221	±120
6.1	253	374	1.53	0.00	8.87	0.0535	4.4	0.301	4.8	0.0408	1.9	0.393	257.8	±4.7	352	±99
7.1	424	592	1.44	0.21	14.60	0.0523	4.0	0.288	4.4	0.03994	1.7	0.396	252.4	±4.3	298	±91
8.1	258	314	1.26	0.58	8.93	0.0501	7.4	0.277	7.6	0.04008	1.9	0.250	253.3	±4.7	198	±170
9.1	577	606	1.09	0.00	20.20	0.0522	2.9	0.293	3.3	0.04077	1.7	0.497	257.6	±4.2	294	±66
10.1	615	887	1.49	0.29	21.50	0.0508	3.9	0.284	4.2	0.04059	1.7	0.395	256.5	±4.2	230	±89
Bt-Am-Ol gabbro-norite (SH105-14)																
1.1	233	274	1.21	0.00	8.36	0.0500	3.4	0.288	3.9	0.04167	2.0	0.511	263.6	±5.2	197	±78
2.1	356	689	2.00	0.00	12.50	0.0518	2.7	0.293	3.3	0.041	1.8	0.560	258.9	±4.7	278	±63
3.1	404	670	1.72	0.00	14.70	0.0517	2.6	0.301	3.2	0.04225	1.8	0.581	266.7	±4.8	272	±59
4.1	699	2082	3.07	0.25	24.80	0.0510	3.0	0.290	3.5	0.04119	1.8	0.507	260.4	±4.6	240	±70
5.1	352	241	0.71	0.00	12.70	0.0511	2.8	0.296	3.4	0.04202	1.9	0.548	265.5	±4.9	246	±65
6.1	393	456	1.20	0.30	14.10	0.0494	4.0	0.284	4.4	0.0417	1.9	0.422	264.1	±4.8	164	±93
7.1	269	357	1.37	0.00	9.77	0.0525	3.2	0.305	3.8	0.04222	2.0	0.531	266.3	±5.3	306	±73
8.1	482	483	1.04	0.24	17.10	0.0511	3.3	0.290	3.8	0.04108	1.8	0.482	259.6	±4.7	246	±77
9.1	220	358	1.68	0.00	7.76	0.0503	4.2	0.285	4.6	0.04111	1.9	0.424	260.1	±5.0	208	±97
10.1	209	359	1.77	0.30	7.57	0.0501	4.7	0.290	5.1	0.04196	2.0	0.386	265.4	±5.2	197	±110

Note. The errors are at the 1 $\sigma$  level. Pbt and Pb\*—total and radiogenic Pb, respectively. The error of standard calibration is no more than 0.51%. Correction for total Pb was made with the measured  $^{204}\text{Pb}$ . Rho—correlation coefficient for  $^{207}\text{Pb}^*/^{235}\text{U}$  and  $^{206}\text{Pb}^*/^{238}\text{U}$ .

The whole-rock Rb-Sr isotope composition was determined in the Analytical Center for multi-elemental and isotope research of IGM SB RAS (Novosibirsk, Russia). The strontium isotopic ratio was measured using the multiple-collector mass-spectrometer MI-1201AT through the double Re-Re tapes. Rb and Sr were extracted with ion chromatography on quartz columns filled with Dowex AG W50x8 resin, the eluent being 2N HCl. The correctness of the  $^{87}\text{Sr}/^{86}\text{Sr}$  ratio was ensured using parallel measurements of each series of water samples according to the VNIIM isotope standard with  $^{87}\text{Sr}/^{86}\text{Sr} = 0.70800 \pm 7$  ( $2\sigma$ ,  $n = 6$ ). The isotope composition of Sr in all of the measured samples was normalized per 0.710248 [51].

Two samples of sulphides (pyrrhotite, chalcopyrite) were analysed for sulphur isotopes. Sulphides were handpicked under a binocular. The separation of  $\text{SO}_2$  from the sulphide mineral for the sulphur isotopic analysis followed the method described in [52]. The sulphur isotopic ratios were determined using a mass spectrometer (Finnigan MAT Delta dual inlet mode) at the Analytical Center for multi-elemental and isotope research of IGM SB RAS in Novosibirsk, Russia. The sulphur isotopic composition is expressed as  $\delta^{34}\text{S}$  (‰) relative to the Canyon Diablo Troilite standard, and its analytical precision is about  $\pm 0.2\text{‰}$ .

## 4. Results

### 4.1. U-Pb Zircon Dating

The zircons in anorthosite (SH220-14/2) and Bt-Am-Ol gabbro-norite (SH105-14) have mostly short prismatic morphologies and euhedral to subhedral crystals. Clear oscillatory zoning, a lack of metamorphic rims and high Th/U ratios indicate a magmatic origin. The locations of the U-Pb spot are shown in Figure 6. The zircons in different samples are similar: the size ranging from 40 to 200  $\mu\text{m}$ , colourless to light yellow or brownish and

transparent to translucent. Isotope parameters and ages of zircons for each sample are shown in Table 2.

Ten zircon grains from SH220-14/2 and ten zircon grains from SH105-14 were analysed with SHRIMP II. These zircons have high U, Th and radiogenic Pb contents of 139–699 ppm, 149–2082 ppm and 5–25 ppm, respectively, with high Th/U ratios of 0.71–3.07. Such Th/U ratios are typical for magmatic rocks [53,54]. SH220-14/2 and SH105-14 yield a mean  $^{206}\text{U}/^{238}\text{Pb}$  age of  $255.8 \pm 2.9$  Ma (MSWD = 0.33) and  $262.6 \pm 3.1$  Ma (MSWD = 0.53), respectively (Figure 6). These zircon U–Pb ages indicate that the mafic rock of the Yamaat Uul complex formed in the Late Permian.

#### 4.2. Mineral Compositions

Olivine occurs in all parts of the Yamaat Uul mafic complex. Its Mg number (Mg#) varies from 68 to 77 in the Central part, from 71 to 72.3 in the Southeastern part and 71–73.6 in the Northwestern part of the complex. Olivine from Intrusion 2 monzogabbro has a lower Mg number of 46–50.3 and higher MnO content than olivine from Intrusion 1 (Figure 7a, Table S1). The CaO and NiO content was rather low: 0.06 to 0.12 wt.% in all rock types.

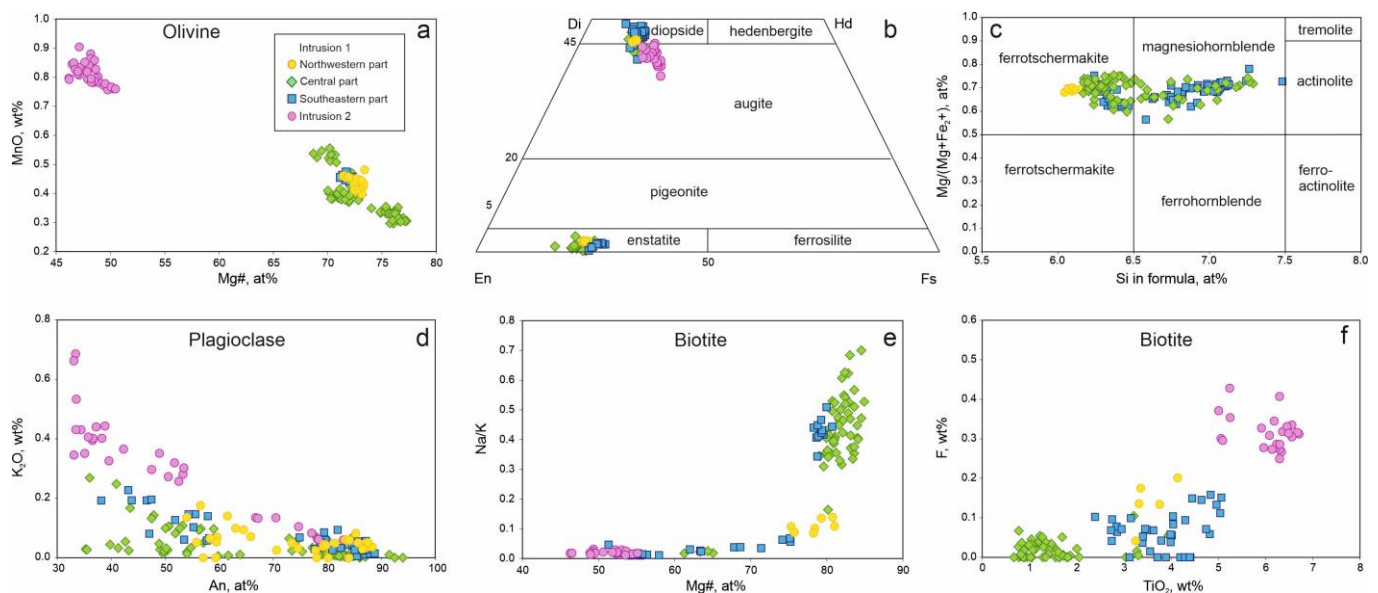


**Figure 7.** Chemical variation plots of olivine (a), clinopyroxene [55] (b), amphibole [56] (c), plagioclase (d) and biotite (e,f) from the studied rocks.

Clinopyroxenes of all parts of the Yamaat Uul complex show similar compositions in the range  $\text{En}_{40-45}\text{Fs}_{8-16}\text{Wo}_{41-49}$  and can be classified as diopside and augite according to the pyroxene nomenclature [55] (Figure 7b, Table S2). Their Mg numbers vary from 73 to 85. Clinopyroxenes are characterized by low  $\text{TiO}_2$  (0.28–1 wt.%) and very low  $\text{Cr}_2\text{O}_3$  (0–0.04%) contents.  $\text{Al}_2\text{O}_3$  and  $\text{Na}_2\text{O}$  contents vary from 0.7 to 5.0 wt.% and 0.15 to 0.65 wt.%, respectively (Table S2). Clinopyroxenes from Intrusion 2 monzogabbro have the composition range  $\text{En}_{39-43}\text{Fs}_{14-21}\text{Wo}_{38-44}$  and are augite [55] (Figure 7b, Table S2). They have a lower Mg number (Mg#, 66–75) and slightly less  $\text{Al}_2\text{O}_3$  content (0.6–2.8 wt.%) compared with clinopyroxenes of gabbroides from Intrusion 1. The compositions of orthopyroxene from all parts of the intrusion fall in the range  $\text{En}_{71-79}\text{Fs}_{20-27}\text{Wo}_{0-2}$  and are classified as enstatite [55] with a Mg# of 72–80 and  $\text{Al}_2\text{O}_3$  (0.9–2.33 wt.%) (Figure 7b, Table S3).

Brown amphibole of Intrusion 1 rocks ranges from magnesiohornblende to tschermakite [56] (Figure 7c). Its Mg number varies from 57 to 75. The composition of this amphibole usually varies within individual samples, particularly in terms of the Mg number and  $\text{TiO}_2$  (0.7–4.6 wt.%) and  $\text{K}_2\text{O}$  (0.3–1.2 wt.%) contents (Table S4).

Plagioclase composition of Intrusion 1 of the Yamaat Uul mafic complex varies within a similar range. It is normally zoned, with An-rich cores gradually passing into An-poor rims (Figure 7d). Cores of plagioclases are generally anorthite–bytownite (An<sub>71–94</sub>) with very low K<sub>2</sub>O content (up to 0.09 wt.%). The maximum of An content (An<sub>91–94</sub>) is observed in gabbroids of the Central part. Plagioclase rims show An content varying from labradorite to andesite (An<sub>35–66</sub>) with K<sub>2</sub>O up to 0.27 wt.%. Plagioclases from monzogabbro of Intrusion 2 have lower An content and correspond to labradorite–bytownite in cores (An<sub>67–83</sub>) and andesite (An<sub>33–53</sub>) in rims. K<sub>2</sub>O content in plagioclase rims is higher than in plagioclase rims from gabbroids and ranges from 0.26 to 0.69 wt.% (Figure 7d, Table S5).

Biotite was observed in all rock types but had different composition in different parts of the complex. In the Central part, it showed a Mg number of 79–85, low T<sub>2</sub>O (0.68–2 wt.%), F (0–0.07 wt.%), high Na<sub>2</sub>O (1.3–2.62 wt.%) and a high N/K ratio (0.3–0.7), with the exception of a few points. Biotites from Southeastern and Northwestern parts have a wide range in the Mg number from 51 to 81, higher TiO<sub>2</sub> (2.4–5 wt.%) content and slightly higher F (up to 0.16 wt.%) content. More magnesian biotite has high Na<sub>2</sub>O (1.55–2.17 wt.%) and a high Na/K ratio (0.3–0.5) like in the Central part; less magnesian minerals have a low Na/K ratio (0.01–0.07) and are richer in K<sub>2</sub>O (7.8–9.7 wt.%) (Supplementary Materials Table S5). Biotite from monzogabbro of Intrusion 2 is characterized by the lowest Mg number varying from 46 to 55 and highest K<sub>2</sub>O (8.9–9.5 wt.%), TiO<sub>2</sub> (5–6.7 wt.%) and F (0.25–0.43 wt.%) contents (Figure 7e,f and Table S6).

#### 4.3. Whole-Rock Geochemistry

Twenty-eight samples of mafic rocks from the Yamaat Uul complex were selected for detailed description (Table 3). The rocks are characterized by a wide range of MgO at variable SiO<sub>2</sub> (Table 3; Figures 8 and 9): SiO<sub>2</sub> spans 39–52 wt.% and MgO from 0.5 to 24.6 wt.%. The ranges of K<sub>2</sub>O, TiO<sub>2</sub> and P<sub>2</sub>O<sub>5</sub> are 0.14–1.87, 0.17–2.01 and 0.03–0.43 wt.%, respectively. The concentrations of Al<sub>2</sub>O<sub>3</sub> and CaO vary in relatively wide ranges of 8.7–30.7 and 4.15–17.1 wt.%, respectively. According to SiO<sub>2</sub> and total alkali (Na<sub>2</sub>O + K<sub>2</sub>O) contents, i.e., the traditional TAS diagram [57], the Yamaat Uul mafic rocks are dominated by gabbro (Figure 8a). The felsic and intermediate surrounding rocks of the Yamaat Uul mafic complex are dominated by monzonite and granite.

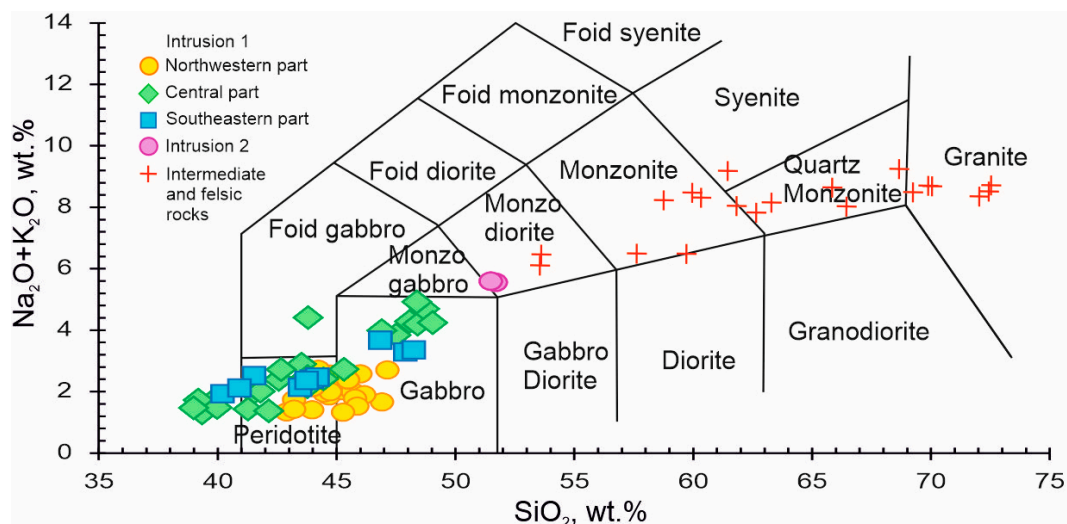


**Figure 8.** Classification diagram for rocks of the Yamaat Uul mafic complex and surrounding rocks (after [57]).

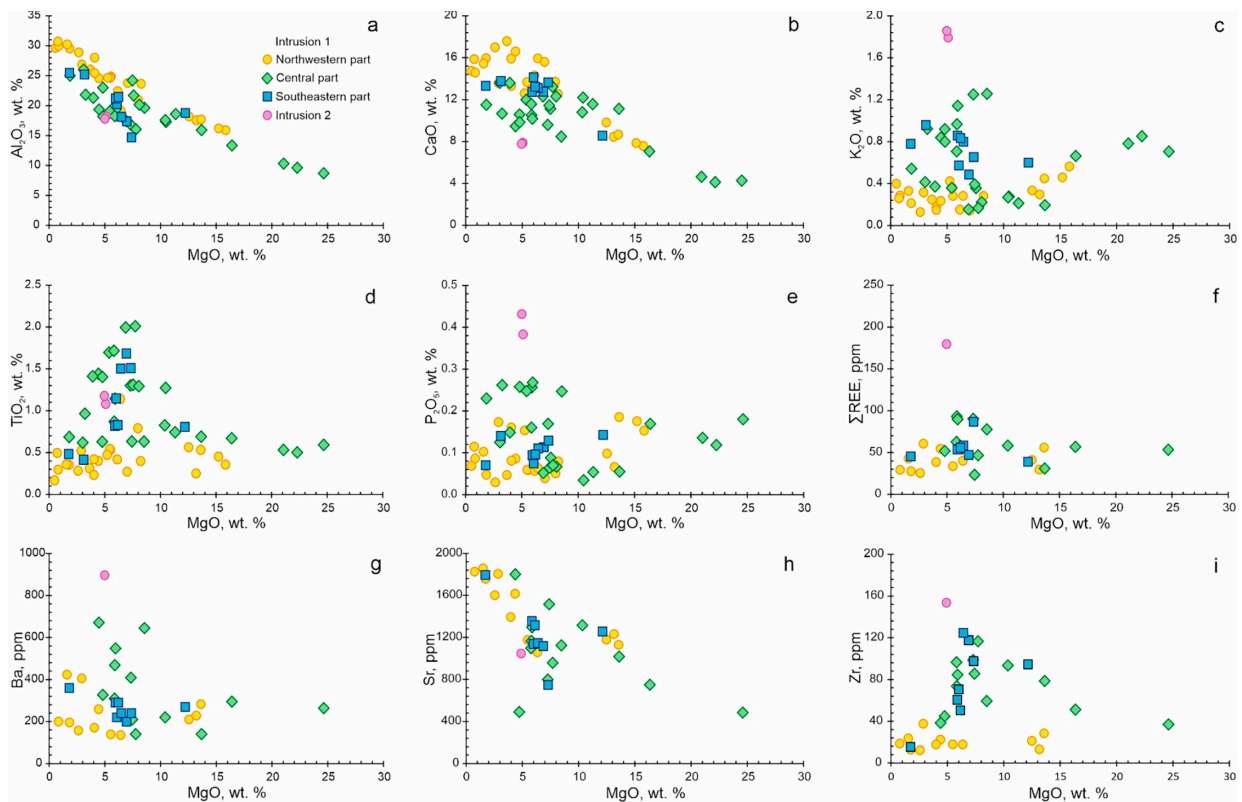


**Figure 9.** Variation diagrams of MgO vs. (a)  $\text{Al}_2\text{O}_3$ , (b) CaO, (c)  $\text{K}_2\text{O}$ , (d)  $\text{TiO}_2$ , (e)  $\text{P}_2\text{O}_5$ , (f)  $\Sigma\text{REE}$ , (g) Ba, (h) Sr and (i) Zr for the mafic rocks from the Yamaat Uul mafic complex.

The rocks of the Northwestern part form two groups on the binary diagrams (Figure 9). The first group is low-K and high-Sr gabbroids (MgO, 0.51–6.41 wt.%;  $\text{K}_2\text{O}$ , 0.12–0.28 wt.%; Sr up to 1831 ppm) represented by leucogabbro and anorthosite (Figure 5c,h). The second group is high-K and low-Sr gabbroids (MgO, 12.53–15.83 wt.%;  $\text{K}_2\text{O}$ , 0.33–0.56 wt.%; 1061–1236 ppm) that are Bt-Am-Ol gabbros and gabbronorites (Figure 5c,h). The rocks of the Southeastern part from the complex are similar in composition to the first group of the Northeastern part, but with less variability.

Monzogabbro is characterized by a high concentration of  $\text{K}_2\text{O}$ ,  $\text{P}_2\text{O}_5$  and  $\Sigma\text{REE}$ : up to 1.87, 0.43 wt.% and 180 ppm, respectively, with 5 wt.% MgO content (Figure 9c,e,f). This is due to the accumulation of incompatible elements during the formation of the mafic complex and the appearance of K-Na feldspar in monzogabbro.

The chondrite-normalized rare-earth element (REE) patterns of the Yamaat Uul complex (Figure 10a,c,e) are flat to moderately enriched in the light REE (LREE):  $\text{La}_n = 5.9\text{--}44.6$ ,  $\text{La}/\text{Sm}_n = 0.9\text{--}4.8$  and  $\text{La}/\text{Yb}_n = 3.9\text{--}16.1$  (Table 3). All samples are characterized by medium-fractionated REE patterns that are slightly depleted in heavy REE (HREE):  $\text{Gd}/\text{Yb}_n = 1.7\text{--}3.0$ . The level of REE concentrations in the monzogabbro of Intrusion 2 (Figure 10a) is higher than that in the rocks of Intrusion 1 (Figure 10a,c,e) in all parts of the complex. The REE patterns of leucogabbro and anorthosite samples of the Northwestern and Southeastern parts show small positive Eu anomalies (Figure 10a,e), suggesting fractionation of plagioclase.

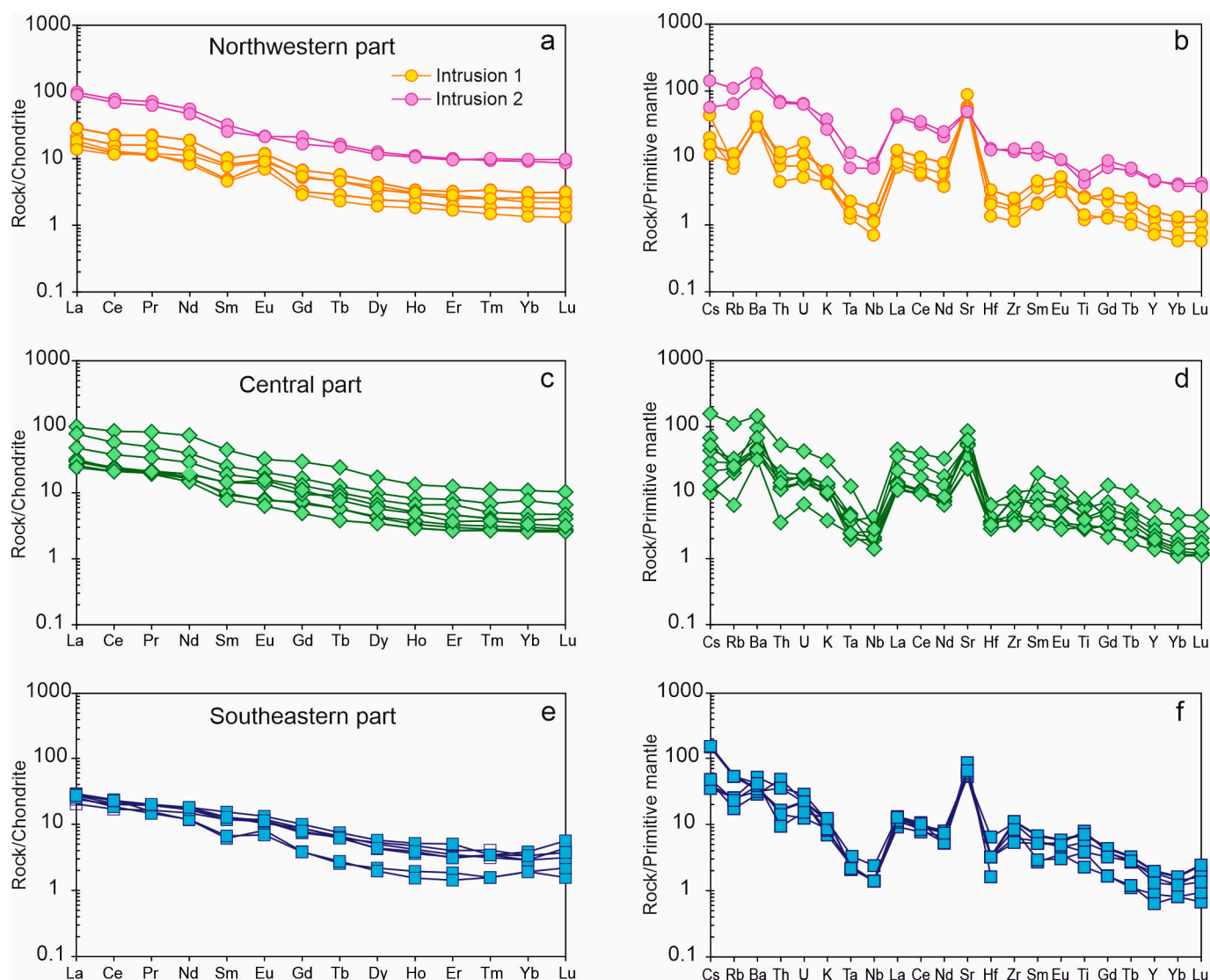


**Figure 10.** CI-chondrite-normalized [48] REE patterns and primitive mantle-normalized [49] trace element spidergrams for the Yamaat Uul mafic complex: (a,b) Northwestern part, (c,d) Central part, (e,f) Southeastern part.

**Table 3.** Representative whole-rock major (wt.%) and trace element (ppm) data for the Yamaat Uul mafic complex.

Intrusion 1										
№	1	2	3	4	5	6	7	8	9	10
Part	NW	NW	NW	NW	NW	NW	NW	NW	NW	NW
Sample	SH100-14	SH102-14	SH103-14	SH105-14	SH220-14/2	SH220-14/10	SH225-14	SH227-14	SH228-14	SH229-14
SiO <sub>2</sub>	44.69	44.01	45.50	43.48	47.14	46.00	43.22	44.72	44.23	46.16
TiO <sub>2</sub>	0.54	0.57	0.25	0.45	0.17	0.30	1.14	0.36	0.53	0.41
Al <sub>2</sub> O <sub>3</sub>	24.81	18.16	17.50	16.18	29.61	29.94	19.14	30.19	26.83	24.54
Fe <sub>2</sub> O <sub>3</sub>	7.37	12.12	10.85	13.33	2.96	4.29	10.91	3.27	5.40	4.24
MnO	0.09	0.16	0.18	0.17	0.02	0.03	0.12	0.06	0.08	0.09
MgO	5.53	12.53	13.20	15.21	0.51	0.84	6.41	1.59	2.91	4.44
CaO	13.70	9.87	8.49	7.90	14.83	14.67	16.02	15.53	13.64	16.69

Table 3. Cont.

Intrusion 1										
Na <sub>2</sub> O	1.57	1.80	2.08	1.72	2.31	2.29	1.14	2.24	2.40	1.66
K <sub>2</sub> O	0.28	0.33	0.29	0.46	0.40	0.28	0.28	0.33	0.31	0.23
P <sub>2</sub> O <sub>5</sub>	0.06	0.10	0.07	0.18	0.07	0.09	0.06	0.10	0.17	0.09
LOI	1.07	0.65	1.36	0.86	1.32	1.09	1.05	1.45	2.13	1.54
Total	99.91	100.59	100.02	100.43	99.55	100.05	99.84	100.05	99.11	100.38
Rb	3.04	5.38	4.44	8.47	6.18	5.26	2.93	5.65	4.72	4.03
Cs	0.18	1.00	0.47	0.36	0.32	0.25	0.29	0.29	0.36	0.25
Ba	138.06	210.14	228.01	267.42	270.44	199.34	134.94	424.08	406.26	259.02
Sr	1178.36	1181.03	1235.58	955.03	1699.40	1831.18	1060.63	1863.81	1810.73	1620.54
Th	0.62	0.64	0.38	0.78	1.34	1.02	0.30	0.78	1.24	1.61
U	0.11	0.16	0.11	0.24	0.39	0.35	0.08	0.24	0.40	0.48
La	4.26	6.55	4.98	8.61	6.46	5.75	4.09	7.67	9.95	8.98
Ce	9.32	13.04	9.77	17.76	12.42	10.46	9.76	15.01	20.20	17.74
Pr	1.45	1.93	1.37	2.23	1.40	1.42	1.61	1.87	2.72	2.31
Nd	6.72	7.81	5.41	9.04	5.31	4.95	7.85	7.76	11.48	9.46
Sm	1.47	1.58	0.94	1.88	0.91	0.89	2.07	1.81	2.46	2.18
Eu	0.67	0.71	0.63	0.67	0.48	0.51	0.81	0.68	0.90	0.82
Gd	1.41	1.34	0.83	1.53	0.79	0.74	2.02	1.24	1.99	1.81
Tb	0.21	0.21	0.13	0.21	0.09	0.11	0.30	0.18	0.25	0.26
Dy	1.23	1.10	0.78	1.04	0.57	0.62	1.77	1.00	1.53	1.49
Ho	0.22	0.21	0.16	0.21	0.11	0.13	0.32	0.18	0.32	0.30
Er	0.59	0.54	0.40	0.56	0.34	0.35	0.78	0.40	0.76	0.79
Tm	0.08	0.08	0.06	0.09	0.05	0.05	0.11	0.06	0.11	0.11
Yb	0.46	0.54	0.38	0.48	0.34	0.28	0.67	0.34	0.65	0.71
Lu	0.07	0.08	0.06	0.07	0.05	0.04	0.10	0.05	0.10	0.11
Zr	17.32	20.69	12.72	35.99	27.48	18.18	17.18	23.01	37.16	21.96
Hf	0.67	0.72	0.42	0.87	0.77	0.62	0.81	0.67	0.99	0.81
Nb	0.57	0.82	0.50	1.23	0.83	0.79	0.47	1.25	1.19	0.64
Ta	<0.05	0.06	<0.05	0.08	0.05	0.06	<0.05	0.05	0.08	<0.05
Y	5.79	5.54	3.95	6.15	3.19	3.22	8.18	4.93	7.43	7.77

Intrusion 1												
N <sup>o</sup>	11	12	13	14	15	16	17	18	19	20	21	22
Part	Central	Central	Central	Central	Central	Central	Central	Central	Central	Central	SE	SE
Sample	SH11-15	SH12-15	SH15-15	SH16-15/1	SH79-16	SH81-16	SH94-16/6	SH97-16	SH98-16/1	SH235-17	SH2-17	SH5-17
SiO <sub>2</sub>	43.67	41.50	48.07	43.80	47.49	46.90	41.80	42.66	43.79	46.83	47.88	40.20
TiO <sub>2</sub>	0.67	0.59	0.63	1.44	0.87	1.15	0.64	1.72	0.83	1.30	0.49	1.69
Al <sub>2</sub> O <sub>3</sub>	13.33	8.67	22.98	19.34	19.92	19.29	24.19	18.22	17.55	16.72	25.45	17.36
Fe <sub>2</sub> O <sub>3</sub>	14.50	15.46	5.95	14.54	8.71	10.44	10.69	15.60	12.43	12.88	6.06	17.74
MnO	0.18	0.20	0.07	0.19	0.12	0.12	0.13	0.14	0.16	0.15	0.07	0.16
MgO	16.39	24.63	4.80	4.45	5.87	5.94	7.44	5.85	10.40	7.32	1.78	6.94
CaO	7.10	4.29	10.64	9.52	10.59	10.24	11.52	11.65	10.87	9.65	13.39	12.84
Na <sub>2</sub> O	1.77	1.24	3.35	3.56	2.86	2.83	1.61	2.00	2.21	2.41	2.50	1.44
K <sub>2</sub> O	0.66	0.71	0.92	0.84	0.97	1.15	0.39	0.71	0.26	1.25	0.78	0.49
P <sub>2</sub> O <sub>5</sub>	0.17	0.18	0.26	-	0.26	0.27	0.06	0.16	-	0.17	0.07	0.11
LOI	0.76	1.82	1.69	0.56	1.26	0.99	1.03	1.09	0.61	0.54	0.52	0.48
Total	99.48	99.64	99.47	99.50	99.05	99.46	99.59	99.96	99.79	99.42	99.08	99.64
Rb	12.59	16.26	17.86	14.58	20.70	27.90	16.20	15.90	4.10	46.90	16.00	11.00
Cs	0.22	1.57	0.67	0.48	1.00	1.80	6.40	1.20	0.30	7.70	0.90	1.00
Ba	295.34	263.56	327.25	673.34	470.00	550.00	210.00	310.00	220.00	410.00	360.00	200.00
Sr	751.59	484.82	490.26	1807.09	1170.00	1300.00	1520.00	1100.00	1320.00	800.00	1800.00	1120.00
Th	0.95	1.04	1.73	0.95	1.40	1.80	10.40	1.20	0.30	5.40	3.00	4.10
U	0.30	0.30	0.39	0.30	0.35	0.42	0.10	0.38	0.14	1.15	0.60	0.46
La	9.40	8.02	9.92	30.95	14.80	14.20	4.50	9.10	7.50	14.00	9.00	6.30
Ce	19.66	17.06	18.72	69.11	30.60	28.90	8.20	18.70	16.90	28.90	19.00	13.70
Pr	2.58	2.41	2.35	10.18	4.10	3.91	1.01	2.59	2.52	3.98	1.90	2.00
Nd	10.26	9.84	8.79	44.10	17.30	17.20	4.20	11.40	11.70	15.60	7.00	8.90
Sm	1.82	1.94	1.52	8.66	3.70	3.40	0.80	2.80	2.80	3.80	1.20	2.30
Eu	0.59	0.56	0.47	2.38	1.19	1.26	0.62	1.01	1.14	1.12	0.60	0.88
Gd	1.78	1.88	1.27	7.64	3.32	3.38	0.68	2.46	2.84	3.45	1.00	2.25
Tb	0.27	0.27	0.18	1.13	0.47	0.46	0.08	0.42	0.36	0.53	0.12	0.31
Dy	1.34	1.40	1.10	5.45	2.51	2.49	0.44	2.08	1.83	2.80	0.70	1.61
Ho	0.24	0.27	0.21	0.95	0.47	0.45	0.06	0.37	0.35	0.48	0.14	0.30
Er	0.63	0.69	0.56	2.60	1.39	1.10	0.28	0.97	0.77	1.35	0.39	0.73
Tm	0.09	0.10	0.09	0.36	0.16	0.16	0.05	0.13	0.12	0.20	0.05	0.10

Table 3. Cont.

Intrusion 1												
Yb	0.57	0.63	0.54	2.26	1.00	1.00	0.20	0.80	0.70	1.30	0.40	0.60
Lu	0.09	0.09	0.08	0.33	0.15	0.21	0.12	0.13	0.10	0.18	0.05	0.14
Zr	50.73	36.49	44.32	37.95	73.00	84.00	85.00	96.00	93.00	98.00	15.00	117.00
Hf	1.15	0.87	1.07	1.33	2.00	1.00	5.00	<1	<1	2.00	0.50	2.00
Nb	1.86	1.36	1.50	3.04	2.00	2.00	1.00	1.00	1.00	3.00	1.70	1.00
Ta	0.10	0.08	0.09	0.15	<0.5	<0.5	1.80	<0.5	<0.5	<0.5	0.60	<0.5
Y	7.62	8.27	6.27	28.31	12.20	11.90	2.20	10.00	8.80	12.80	4.00	7.20

№	Intrusion 1				Intrusion 2		Felsic and Intermediate Rocks					
	SE	SE	SE	SE	NW	NW	30	31	32	33	34	
Part	SE	SE	SE	SE	NW	NW	30	31	32	33	34	
Sample	SH7-17	SH14-17	SH231-17	SH232-17	SH234-14	SH235-14	SH10-15	SH16-17	SH17-17	PM30-16	SH80-16	SH17-15
SiO <sub>2</sub>	43.45	43.96	40.91	44.19	51.70	51.50	58.76	60.31	59.95	65.85	69.89	61.45
TiO <sub>2</sub>	1.15	1.51	0.81	0.82	1.08	1.18	0.97	0.79	0.81	0.49	0.33	0.76
Al <sub>2</sub> O <sub>3</sub>	20.21	14.66	18.73	21.17	18.14	17.77	16.76	16.65	16.75	16.44	14.84	17.53
Fe <sub>2</sub> O <sub>3</sub>	11.60	15.07	15.81	9.83	9.41	9.96	6.57	6.17	5.87	3.47	2.57	4.79
MnO	0.12	0.21	0.16	0.11	0.14	0.15	0.11	0.10	0.09	0.06	0.05	0.10
MgO	6.04	7.36	12.19	5.92	5.09	4.98	2.44	2.38	2.46	1.02	0.64	1.68
CaO	14.20	13.73	8.62	12.80	7.92	7.82	4.39	4.23	4.26	2.58	1.66	3.31
Na <sub>2</sub> O	1.56	1.74	1.51	1.60	3.75	3.73	3.99	3.91	4.02	4.45	4.01	4.80
K <sub>2</sub> O	0.57	0.65	0.60	0.86	1.80	1.87	4.23	4.39	4.44	4.18	4.69	4.37
P <sub>2</sub> O <sub>5</sub>	0.07	0.13	0.14	0.09	0.38	0.43	0.31	0.33	0.33	0.16	0.10	0.30
LOI	0.41	0.36	0.07	1.65	0.00	-0.25	0.44	0.26	0.23	0.51	0.52	0.19
Total	99.55	99.59	99.77	99.30	99.63	99.32	99.16	99.68	99.35	99.42	99.47	99.52
Rb	16.00	19.60	14.60	33.80	69.61	41.05	127.14	198.00	226.00	-	-	105.88
Cs	0.80	0.90	1.10	3.50	3.27	1.31	2.58	8.60	9.90	-	-	2.43
Ba	220.00	240.00	270.00	290.00	1283.86	898.84	1231.56	840.00	820.00	-	-	1497.41
Sr	1140.00	750.00	1260.00	1360.00	1023.55	1047.67	697.31	680.00	670.00	-	-	579.05
Th	3.00	1.80	1.20	0.80	5.98	5.65	13.74	25.90	32.00	-	-	13.34
U	0.45	0.89	0.26	0.32	1.37	1.33	1.40	3.85	4.05	-	-	2.39
La	7.40	12.20	7.90	8.80	27.90	30.62	37.00	39.30	43.30	-	-	41.64
Ce	16.20	26.20	14.90	18.20	55.61	62.54	71.89	74.60	84.40	-	-	79.83
Pr	2.36	3.57	1.78	2.38	7.62	8.72	8.99	9.26	10.10	-	-	9.78
Nd	10.00	15.40	7.10	10.00	27.85	33.27	32.28	33.60	36.60	-	-	35.56
Sm	2.50	3.90	1.30	2.30	4.96	6.27	5.41	6.60	6.70	-	-	5.95
Eu	0.76	1.22	0.51	0.82	1.57	1.59	1.20	1.41	1.50	-	-	1.55
Gd	2.28	3.63	0.99	1.92	4.24	5.46	4.85	5.23	5.44	-	-	5.03
Tb	0.29	0.53	0.13	0.30	0.70	0.77	0.72	0.73	0.81	-	-	0.75
Dy	1.71	2.71	0.63	1.37	3.69	4.03	3.97	3.68	3.99	-	-	4.10
Ho	0.34	0.53	0.11	0.26	0.75	0.79	0.72	0.69	0.74	-	-	0.74
Er	0.84	1.51	0.30	0.67	1.99	2.10	2.09	2.02	2.06	-	-	2.27
Tm	0.13	0.19	0.05	0.11	0.32	0.30	0.33	0.30	0.35	-	-	0.36
Yb	0.70	1.20	0.40	0.60	2.02	1.90	1.94	2.10	2.30	-	-	2.15
Lu	0.12	1.19	0.07	0.10	0.31	0.28	0.29	0.34	0.36	-	-	0.33
Zr	70.00	97.00	94.00	60.00	138.36	152.81	213.71	62.00	57.00	-	-	319.27
Hf	1.00	2.00	<1	<1	4.28	4.03	4.90	8.00	8.00	-	-	7.68
Nb	1.00	1.00	1.00	1.00	5.85	4.98	8.82	10.00	13.00	-	-	7.93
Ta	<0.5	<0.5	<0.5	<0.5	0.48	0.28	0.55	<0.5	0.70	-	-	0.51
Y	8.40	13.00	2.90	6.00	20.31	21.32	23.84	19.80	20.40	-	-	22.74

The primitive mantle normalized multi-element patterns for all samples (Figure 10 b,d,f) show a clear Nb, Zr and Hf depletion (Table 3). The presence of the Nb and Hf minimums is a typical feature of rocks formed in a subduction-related setting. All samples are characterized by enrichment in LREE and Sr of varying intensity. The Sr maximum shows fractionation of plagioclase. Generally, the level of the trace element in the monzogabbro of Intrusion 2 (Figure 10b) is higher than that in the rocks of Intrusion 1 (Figure 10b,d,f) in all parts of the complex.

#### 4.4. Whole-Rock Nd, Sr and S Isotopes

Whole-rock Sr-Nd isotopic compositions for selected samples from the mafic rocks of the Yamaat Uul complex and monzodiorite are given in Table 4. The initial  $^{87}\text{Sr}/^{86}\text{Sr}$  ratios ( $I_{\text{Sr}}$ ) and  $\epsilon\text{Nd}(t)$  values were calculated on the basis of the zircon U-Pb ages for these rocks

(~260 Ma). The  $\epsilon\text{Nd}(t)$  values for the mafic rocks range from  $-0.05$  to  $+1.79$ . Their  $I_{\text{Sr}}$  values range from  $0.70458$  to  $0.70500$ . In contrast, the  $\epsilon\text{Nd}(t)$  values for the quartz monzodiorites range from  $0.41$  to  $+5.72$ , apparently higher than those of mafic rocks (Figure 11). Their  $I_{\text{Sr}}$  values range from  $0.70477$  to  $0.70497$ .

**Table 4.** Sr–Nd isotopic data of mafic rocks from the Yamaat Uul mafic complex and environs.

Sample №	$^{87}\text{Rb}/^{86}\text{Sr}$	$^{87}\text{Sr}/^{86}\text{Sr}$	$\pm 2\sigma$	$I_{\text{Sr}}$	$^{147}\text{Sm}/^{144}\text{Nd}$	$^{143}\text{Nd}/^{144}\text{Nd} \pm 2\sigma$	$\epsilon\text{Nd}(0)$	$\epsilon\text{Nd}(t)$	
1 SH220-14/10	0.00794	0.704690	0.00002	0.70466	0.10872	0.512550	0.0003	−1.71	1.21
2 SH105-14	0.02233	0.704660	0.00004	0.70458	0.11756	0.512595	0.0003	−0.84	1.79
3 SH225-14	0.00771	0.704650	0.00002	0.70462	0.16622	0.512660	0.0005	0.42	1.43
4 SH12-15	0.09682	0.705170	0.00004	0.70481	0.12964	0.512563	0.0003	−1.46	0.76
5 SH2-17	0.04698	0.705191	0.00002	0.70502	0.11153	0.512505	0.0003	−2.59	0.24
6 SH7-17	0.05247	0.705196	0.00001	0.70500	0.14538	0.512606	0.0004	−0.62	1.08
7 SH231-17	0.03658	0.705136	0.00001	0.70500	0.10104	0.512473	0.0003	−3.22	−0.05
8 SH235-14	0.10768	0.705370	0.00003	0.70497	0.11845	0.512520	0.0003	−2.30	0.30
9 SH10-15	0.61153	0.707030	0.00002	0.70477	0.11150	0.512514	0.0003	−2.42	0.41
10 SH16-17	0.87250	0.708195	0.00001	0.70497	0.10834	0.512781	0.0003	2.78	5.72

Note: the  $I_{\text{Sr}}$  and  $\epsilon\text{Nd}(t)$  values of the Yamaat Uul mafic complex were calculated at the age of 260 Ma.

The sulphide in the rocks of the Yamaat Uul mafic complex have  $\delta^{34}\text{S}$  values ranging from  $+0.8$  (SH222-14) to  $+1.1$  (SH220-14/10), which are within the typical mantle range [58,59].

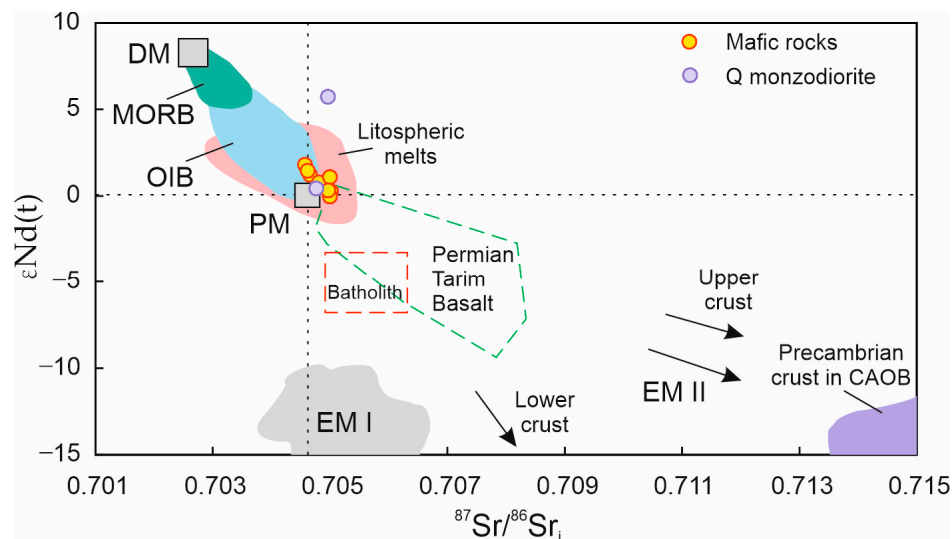


**Figure 11.** Plot of  $\epsilon\text{Nd}(t)$  and initial  $^{87}\text{Sr}/^{86}\text{Sr}$  values for the mafic rocks and Q monzodiorites of the Yamaat Uul mafic complex. DM, depleted mantle; MORB, middle ocean ridge basalt; OIB, ocean island basalt; PM, primitive mantle; EM I and EM II, enriched mantle 1 and 2 sources. Data sources: fields for DM, PM, MORB and OIB are from [60]; field for regional lithospheric melts is based on the data from [61]; Permian Tarim basalt is from [12]; the Precambrian CAOB crust and batholith are from [27].

## 5. Discussion

### 5.1. Age of Rock Formation

The geological maps of the Khangai Mountains in previous studies show that all mafic–ultramafic intrusions are of an Early Palaeozoic age [62,63]. All isolated zircons from the rocks of the Yamaat Uul mafic complex are Permian (255–262 Ma), and all zircons are magmatic, while none are xenogenic (Figure 6 and Table 3).

Thus, the data obtained allow us to date the formation of the Yamaat Uul complex to the Permian (255–262 Ma) rather than to the Early Palaeozoic as previously thought [62,63]. The following mafic–ultramafic intrusions of the Khangai Mountains formed during the

same time interval: the Nomgon troctolite–anorthosite–gabbro intrusion ( $256 \pm 2.1$  Ma) [30], the Oortsog Uul peridotite–troctolite–gabbro intrusion (257–278 Ma) [32], the Dzaraa Uul monzogabbro intrusion (269 Ma) [15] and the Nariintolburingol intrusion (249–252 Ma) [63]. The rocks of some of them are enriched in PGE [16,32,64]. There is every reason to suggest that the Yamaat Uul complex together with the forenamed intrusions of Mongolia, localized in the single CAOBS structure, are the products of Permian magmatism belonging to a single igneous province.

The Yamaat Uul mafic complex is associated with the Early Permian bimodal volcano–plutonic complex [65]. According to [66], such bimodal complexes are the result of riftogenesis initiated by plume activity (Khangai plume), superimposed on the environment of the active continental margin. Thus, the Yamaat Uul complex, as well as other Permian mafic–ultramafic intrusions of Western Mongolia, was formed during the formation of the Khangai batholith (~270–240 Ma) [26], as its earlier intrusion portion [67].

### 5.2. Source Mantle Characteristics and Crustal Contamination

The Yamaat Uul mafic complex has some unique chemical (geochemical) characteristics compared to other mafic complexes in the world. In our opinion, the MgO–K<sub>2</sub>O diagram is the most informative. In general, the potassium content in the rocks of the layered complexes increases monotonously as the magnesium content in the rocks increases, for example, in the Skye and Skaergaard mafic complexes [68] (Figure 12). The potassium content in the rocks of the complex does not increase monotonously with decreasing magnesium content in the rocks, but one has a decrease in the plagioclase cumulates in the Yamaat Uul complex on the diagram (Figures 9c and 12). The same distribution of rock compositions is observed in the Oortsog Uul intrusion of the Khangai Mountains [17] and in the Yoko–Dovyren complex of northern Transbaikalia [69]. This distribution can be explained by the following: 1. Two melts (as in the case of the Oortsog Uul complex) and 2. Different contents of trapped melts in plagioclase and olivine–pyroxene cumulates.

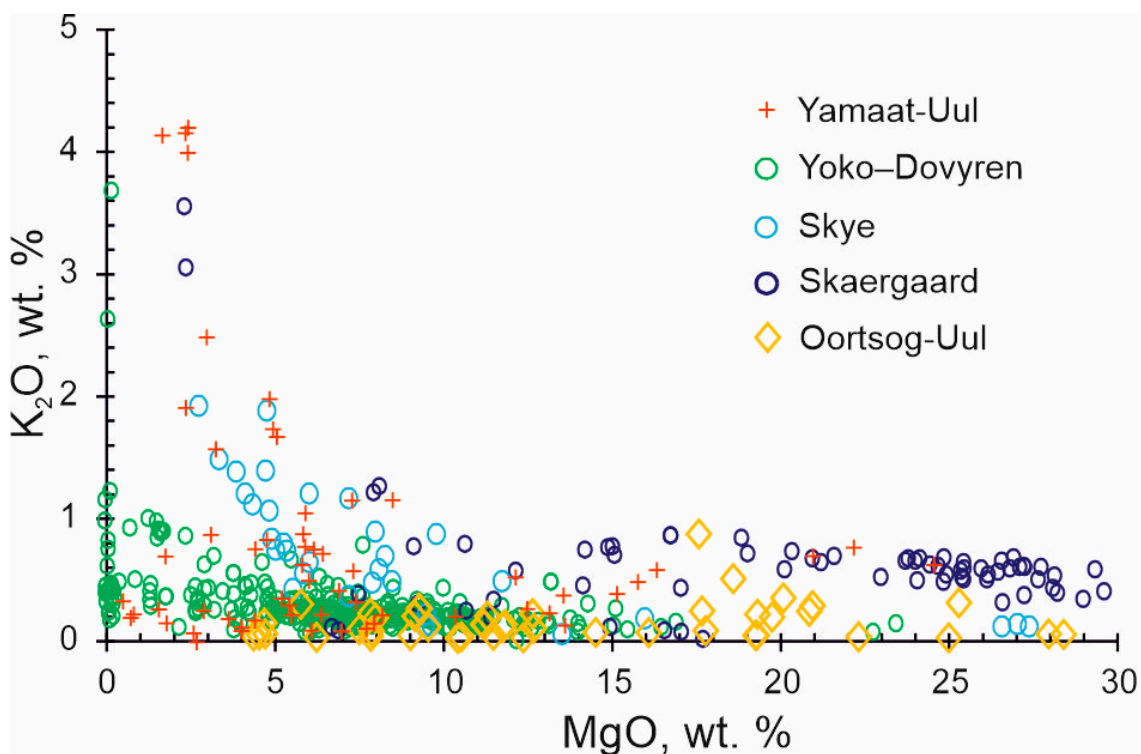


**Figure 12.** Comparison of MgO vs. K<sub>2</sub>O content in the Yamaat Uul mafic complex and layered intrusions: Yoko–Dovyren [69], Skye, Skaergaard [68], Oortsog Uul [17].

The Yamaat Uul mafic complex is similar to the Oortsog Uul peridotite–troctolite–gabbro intrusion [17] in terms of age, mineralogy and geochemistry. Primary amphibole and biotite with high  $\text{TiO}_2$  contents (Bt—0.68–5.07 and 3.00–3.01 wt.%, Am—0.23–4.60 and 0.65–3.21 wt.% for Yamaat Uul and Oortsog Uul, respectively) occur in rocks of both intrusions at later stages of formation. Plagioclases have a high An content (75–94% and 81–97%, respectively), and olivine and clinopyroxene have a similar composition. The two intrusions are characterised by rocks with high MgO values: 12.59–25.27 wt.% (Oortsog Uul) and 12.54–25.17 wt.% (Yamaat Uul). These are enriched in  $\text{K}_2\text{O}$  (0.20–0.87 and 0.30–0.87 wt.%, respectively). The same pattern is observed for  $\text{TiO}_2$ ,  $\text{P}_2\text{O}_5$  and  $\text{Na}_2\text{O} + \text{K}_2\text{O}$ ; there is an enrichment in incompatible elements with an increase in MgO. The rocks of the early intrusions of Oortsog Uul and Yamaat Uul show a gradual increase in the Eu maximum on REE patterns, HFSE (Ta, Nb, Zr, Hf) depletion and LILE (Ba, K) enrichment on spidergrams; therefore, they have typomorphic features of mafic magmas that are subduction-related [70].

Thus, the Permian Yamaat Uul and Oortsog Uul intrusions have similar characteristics. However, Oortsog Uul consists of two intrusions formed from two different melts with different contents of incompatible elements: K, Ti, P and REE. It has been shown that the enriched melt was involved in the formation of Intrusion 1 of the Oortsog Uul, while the depleted melt was involved in the formation of Intrusion 2 [17]. The Sm–Nd isotope composition data (Table 4) confirm the single source of rock formation in the Yamaat Uul complex. The rocks of Intrusions 1 and 2 have close  $\epsilon\text{Nd}$  values (0.30 and 1.79, respectively), while for Intrusions 1 and 2 of Oortsog Uul, they have different  $\epsilon\text{Nd}$  values (+11 and –3.6, respectively) [17]. Spidergrams of rocks from the Yamaat Uul and Oortsog Uul intrusions show different Sr contents (50.3–88.3 and 1.2–18.6, respectively) at similar MgO contents. This suggests that the Sr content of the mantle is highly variable; there is mantle heterogeneity beneath Khangai in the Permian.

The high Sr content in the rocks of the Yamaat Uul complex (Figure 10, Table 3) may be due to crustal contamination. Since all the zircons are magmatic and xenogenic zircons are absent (see Figure 6a,b), crustal contamination is not typical for the rocks of the Yamaat Uul complex. Furthermore, the  $\delta^{34}\text{S}$  values of the sulphide mineralization from Yamaat Uul are from 0.8 to 1.1‰, which are within the typical mantle range [58]. Similar  $\delta^{34}\text{S}$  values are typical for disseminated ores of the Gorozubovsky intrusion (2.7‰) [71], and the Zub-Marksheider intrusion (0.39‰) [72] in the Permian–Triassic Noril'sk Province (Russia). These values suggest that “mantle-like” S isotopic composition reflects the primary sulphide assemblage that has not been changed with interaction in a deep-staging chamber, during passage to the surface, or with in situ assimilation, as is frequently suggested [73,74]. The lack of evidence for crustal contamination of the parental magma is also supported with Sr–Nd isotopic data from the Yamaat Uul complex. As shown in Figure 11, the gabbroids show little variation in the isotopic compositions  $I_{\text{Sr}}$  and  $\epsilon\text{Nd}(t)$ , and correspond to the field of the lithospheric mantle under the CAO [61]. Therefore, crustal contamination is not characteristic of the rocks of the Yamaat Uul mafic complex.

### 5.3. PGE Depletion in Parental Magma

Mantle heterogeneity in the Permian may have influenced the development of metallogeny in the Khangai region. There are mafic–ultramafic intrusions with PGE–Cu–Ni mineralization in the Khangai Mountains, Oortsog Uul and Nomgon [32,63], which, together with the studied intrusion, belong to a single metallogenic province formed above the Khangai plume [24,32].

The different degrees of sulphide melt fractionation of the Nomgon, Oortsog Uul and Yamaat Uul intrusions are clearly shown in the diagram (Figure 13a) and are due to positive correlation or joint enrichment of the melt with copper and PGE (Figure 13b). The sulphide melt fractionates with enrichment of PGE in the Oortsog Uul and Nomgon intrusions, reaching high values that lead to the formation of PGE mineralization that has been detected in these intrusions [32]. On the other hand, no such correlation is found

in the Yamaat Uul complex: PGE does not accumulate with increasing Cu. Therefore, a bornite–cubanite–chalcopyrite association of sulphides appears in the complex, but PGMs are not detected, compared with the Nomgon intrusion.

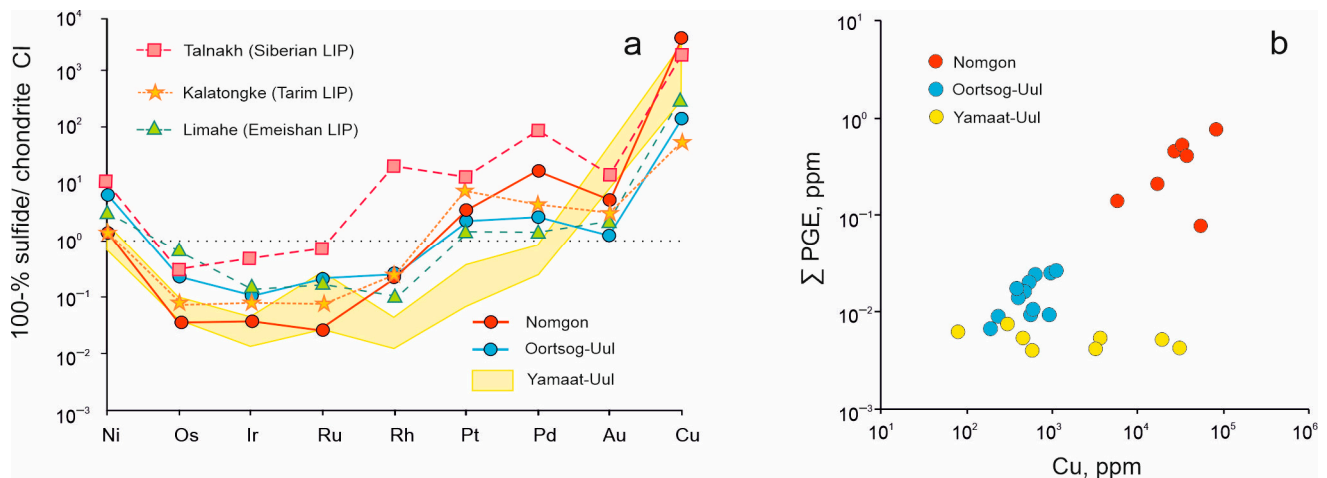


**Figure 13.** (a) Chondrite-normalized [75] chalcophile element distribution patterns for the Yamaat Uul complex in comparison with intrusions of the Khangai Mountains (Nomgon, Oortsog Uul [32]) and disseminated ores of other deposits related to LIPs (Talnakh [43], Kalatongke [76], Limahe [10]). All compositions were recalculated to 100% sulphide. (b) Correlation of  $\Sigma$ PGE vs. Cu for Yamaat Uul complex compared to intrusions of the Khangai Mountains (after [32]).

Three possible factors contribute to the PGE depletion in the parental magmas: (1) a PGE-depleted source mantle; (2) a low degree of partial melting of the PGE-undepleted mantle; or (3) previous sulphide removal in the staging magma chamber prior to the emplacement of the parental magmas. The sulphide mineralization from Oortsog Uul and Nomgon shows no obvious PGE depletion [32], suggesting a PGE-undepleted mantle source in the Khangai region.

The IPGE and Ni are more compatible than the PPGE and Cu during partial melting of the mantle [77]. Therefore, a high degree of partial melting of the mantle would result in high Ni/Cu and low Pd/Ir ratios. The sulphide mineralization from the Yamaat Uul complex has moderate Ni/Cu and Pd/Ir ratios, ranging from 0.9 to 10.8 and from 10.7 to 50.5, respectively, and is related to the field of high-Mg basalts and layered intrusions [32]. Sulphide mineralization from the Yamaat Uul complex is apparently depleted in PGE relative to Cu (and Ni) (Figure 13b). In addition, compared to the important Ni-Cu (-PGE) deposits in the LIPs of the Eurasian plate, the sulphide mineralization of the Yamaat Uul complex (in 100% sulphide) has slightly lower Ni contents and significant PGE depletion (Figure 13).

Parental magmas with Cu/Pd ratios higher than the mantle value of ~7000 [78] may reflect the sulphide removal at depth [76,79]. The sulphide mineralization of the Yamaat Uul intrusion has much higher Cu/Pd ratios (10163–1375726) than the mantle value [32], further indicating sulphide removal from primary magmas prior to intrusion emplacement. In conclusion, the PGE depletion of parental magmas in the Yamaat Uul complex may be due to sulphide removal at a deep staging magma chamber or low degrees of partial melting of the mantle source of the Yamaat Uul complex.

## 6. Conclusions

- (1) Zircon U-Pb dating (SHRIMP II) of the anorthosite and Bt-Am-Ol gabbro-norite of the Yamaat Uul mafic complex in the Khangai Mountains has a revealed age of  $255.8 \pm 2.9$  Ma and  $262.6 \pm 3.1$  Ma, respectively. Thus, the mafic rocks of the complex were formed in the Late Permian and, together with other mafic-ultramafic intrusions of the Khangai Mountains, are early phases of the Khangai batholith.

- (2) The Yamaat Uul mafic complex consists of two intrusions; Intrusion 1 is represented by plagioclase cumulates and olivine–pyroxene cumulates and Intrusion 2 is composed of monzogabbro. All of the rocks of the complex are derived from a unified parental melt due to different amounts of trapped melts in plagioclase and olivine–pyroxene cumulates.
- (3) Magmatic zircons, Sm–Nd, Rb–Sr isotope data and sulphur isotopes indicate that crustal contamination did not affect the formation of the Yamaat Uul mafic complex.
- (4) The Yamaat Uul mafic complex together with other mafic–ultramafic intrusions of the Khangai Mountains are related to the Khangai LIP and can be considered as potential for the PGE–Cu–Ni. These intrusions have a low degree of evolution of the sulphide melt.

**Supplementary Materials:** The following supporting information can be downloaded at: <https://www.mdpi.com/article/10.3390/min13060833/s1>, Table S1: Representative olivine compositions of the Yamaat Uul mafic complex; Table S2: Representative clinopyroxene compositions of the Yamaat Uul mafic complex; Table S3: Representative orthopyroxene compositions of the Yamaat Uul mafic complex; Table S4: Representative amphibole compositions of the Yamaat Uul mafic complex; Table S5: Representative plagioclase compositions of the Yamaat Uul mafic complex; Table S6: Representative biotite compositions of the Yamaat Uul mafic complex.

**Author Contributions:** Conceptualization, methodology, review and editing, R.S.; writing—original draft preparation, visualization, funding acquisition, M.S.; mineralogy, validation, V.E.; sampling, preparation and description, Y.S.; sampling, field trip, T.-U.O.; editing, N.T. All authors have read and agreed to the published version of the manuscript.

**Funding:** The reported study was funded by Russian Science Foundation, No. 22-77-00058, <https://rscf.ru/en/project/22-77-00058/>, accessed on 14 June 2023.

**Data Availability Statement:** Not applicable.

**Acknowledgments:** We are grateful to A. Izokh, M. Podlipsky and S. Rudnev for providing samples, assistance in field work and advice. We thank analysts O. Khmelnikova, V. Kiseleva, N. Karmanova and I. Nikolaeva for carrying out analytical procedures, and N. Belkina for technical assistance in preparing the manuscript.

**Conflicts of Interest:** The authors declare no conflict of interest. The funders had no role in the design of the study; in the collection, analyses or interpretation of data; in the writing of the manuscript; or in the decision to publish the results.

## References

1. Ernst, R. *Large Igneous Provinces*, 1st ed.; Cambridge University Press: Cambridge, UK, 2014; p. 666.
2. Mekhonoshin, A.S.; Kolotilina, T.B. Petrological-geochemical features of ultrabasites from the southern framing of the Siberian craton and exploration criteria for Ni sulfide ores. *Ores Met.* **2006**, *6*, 26–30.
3. Tolstykh, N.D.; Orsoev, D.A.; Krivenko, A.P.; Izokh, A.E. *Precious Metal Mineralization in Layered Ultramafic-Mafic Massifs in the South of the Siberian Platform*, 1st ed.; Parallel: Novosibirsk, Russia, 2008; p. 194.
4. Polyakov, G.V.; Izokh, A.E.; Borisenko, A.S. Permian ultramafic-mafic magmatism and accompanying Cu–Ni mineralization in the Gobi-Tien Shan belt as a result of the Tarim plume activity. *Russ. Geol. Geophys.* **2008**, *49*, 455–467. [[CrossRef](#)]
5. Polyakov, G.V.; Tolstykh, N.D.; Mekhonoshin, A.S.; Izokh, A.E.; Podlipkii, M.Y.; Orsoev, D.A.; Kolotilina, T.B. Ultramafic-mafic igneous complexes of the Precambrian East Siberian metallogenic province (southern framing of the Siberian craton): Age, composition, origin and ore potential. *Russ. Geol. Geophys.* **2013**, *54*, 1319–1331. [[CrossRef](#)]
6. Wang, C.Y.; Wei, B.; Zhou, M.-F.; Minh, D.H.; Qi, L. A synthesis of magmatic Ni–Cu–(PGE) sulfide deposits in the ~260 Ma Emeishan large igneous province, SW China and northern Vietnam. *J. Asian Earth Sci.* **2018**, *154*, 162–186. [[CrossRef](#)]
7. Hoa, T.T.; Izokh, A.E.; Polyakov, G.V.; Borisenko, A.S.; Anh, T.T.; Balykin, P.A.; Phuong, N.T.; Rudnev, S.N.; Van, V.V.; Nien, B.A. Permo-Triassic magmatism and metallogeny of Northern Vietnam in relation to the Emeishan plume. *Russ. Geol. Geophys.* **2008**, *49*, 480–491. [[CrossRef](#)]
8. Svetlitskaya, T.V.; Nevolko, P.A.; Ngo, T.P.; Tran, T.H.; Izokh, A.E.; Shelepaev, R.A.; Bui, A.N.; Vu, H.L. Small-intrusion-hosted Ni–Cu–PGE sulfide deposits in northeastern Vietnam: Perspectives for regional mineral potential. *Ore Geol. Rev.* **2017**, *86*, 615–623. [[CrossRef](#)]

9. Svetlitskaya, T.V.; Ngo, T.H.; Nevolko, P.A.; Tran, T.A.; Izokh, A.E.; Shelepaev, R.A.; Tran, T.H.; Ngo, T.P.; Fominykh, P.A.; Pham, N.C. Zircon U-Pb ages of Permian-Triassic igneous rocks in the Song Hien structure, NE Vietnam: The Emeishan mantle plume or the Indosinian orogeny? *J. Asian Earth Sci.* **2022**, *224*, 105033. [[CrossRef](#)]
10. Tao, Y.; Li, C.; Song, X.; Ripley, E.M. Mineralogical, petrological and geochemical studies of the Limahe mafic-ultramafic intrusion and the associated Ni-Cu sulfide ores, SW China. *Miner. Deposit.* **2008**, *43*, 849–872. [[CrossRef](#)]
11. Zhou, M.F.; Arndt, N.T.; Malpas, J.; Wang, C.Y.; Kennedy, A.K. Two magma series and associated ore deposit types in the Permian Emeishan large igneous province, SW China. *Lithos* **2008**, *103*, 352–368. [[CrossRef](#)]
12. Tang, D.M.; Qin, K.Z.; Li, C.S.; Qi, L.S.; Su, B.X.; Qu, W.J. Zircon dating, Hf-Sr-Nd-Os isotopes and PGE geochemistry of the Tianyu sulfide-bearing mafic-ultramafic intrusion in the Central Asian Orogenic Belt, NW China. *Lithos* **2011**, *126*, 84–98. [[CrossRef](#)]
13. Luo, W.; Zhanga, Z.; Santosha, M.; Houa, T.; Huanga, H.; Zhua, J.; Wanga, X.; Fua, X. Petrology and geochemistry of Permian mafic-ultramafic intrusions in the Emeishan large igneous province, SW China. *Ore Geol. Rev.* **2014**, *56*, 258–275. [[CrossRef](#)]
14. Wang, Z.-Z.; Han, B.-F.; Feng, L.-X.; Liu, B. Geochronology, geochemistry and origins of the Paleozoic-Triassic plutons in the Langshan area, western Inner Mongolia, China. *J. Asian Earth Sci.* **2015**, *97*, 337–351. [[CrossRef](#)]
15. Izokh, A.E.; Vishnevskii, A.V.; Polyakov, G.V.; Shelepaev, R.A. Age of picrate and picrodolerite magmatism in Western Mongolia. *Russ. Geol. Geophys.* **2011**, *52*, 7–23. [[CrossRef](#)]
16. Mao, Y.J.; Dash, B.; Qin, K.Z.; Bujinlkham, B.; Tang, D.M. Comparisons among the Oortsog, Dulaan, and Nomgon mafic-ultramafic intrusions in central Mongolia and Ni-Cu deposits in NW China: Implications for economic Ni-Cu-PGE ore exploration in central Mongolia. *Russ. Geol. Geophys.* **2018**, *59*, 1–18. [[CrossRef](#)]
17. Shapovalova, M.O.; Tolstykh, N.D.; Shelepaev, R.A.; Tsibizov, L.V. The Oortsog Peridotite-Troctolite-Gabbro Intrusion, Western Mongolia: New Petrological and Geochronological Constraints. *Russ. Geol. Geophys.* **2019**, *60*, 845–861. [[CrossRef](#)]
18. Borisenko, A.S.; Sotnikov, V.I.; Izokh, A.E.; Polyakov, G.V.; Obolensky, A.A. Permo-triassic mineralization in Asia and its relation with plume magmatism. *Russ. Geol. Geophys.* **2006**, *47*, 170–186.
19. Zhang, C.L.; Li, Z.X.; Li, X.H.; Xu, Y.G.; Zhou, G.; Ye, H.M. A Permian large igneous province in Tarim and Central Asia orogenic belt, NW China: Results of aca. Ma mantle plume? *Geol. Soc. Am. Bull.* **2010**, *122*, 2020–2040. [[CrossRef](#)]
20. Xu, Y.-G.; Wei, X.; Luo, Z.-Y.; Liu, H.; Cao, J. The Early Permian Tarim Large Igneous Province: Main characteristics and a plume incubation model. *Lithos* **2014**, *204*, 20–35. [[CrossRef](#)]
21. Dobretsov, N.L. 250 Ma large igneous provinces of Asia: Siberian and Emeishan traps (plateau basalts) and associated granitoids. *Russ. Geol. Geophys.* **2005**, *46*, 870–890.
22. Yarmolyuk, V.V.; Kovalenko, V.I. Deep geodynamics and mantle plumes: Their role in the formation of the Central Asian orogenic belt. *Petrology* **2003**, *11*, 504–531.
23. Bryan, S.E.; Ernst, R.E. Revised definition of large igneous provinces (LIPs). *Earth Sci. Rev.* **2008**, *86*, 175–202. [[CrossRef](#)]
24. Yarmolyuk, V.V.; Kozlovsky, A.M.; Kuzmin, M.I. Zoned magmatic areas and anorogenic batholith formation in the Central Asian Orogenic Belt (by the example of the Late Paleozoic Khangai magmatic area). *Russ. Geol. Geophys.* **2016**, *57*, 357–370. [[CrossRef](#)]
25. Yarmolyuk, V.V.; Kozlovsky, A.M.; Sal'nikova, E.B.; Kozakov, I.K.; Kotov, A.B.; Lebedev, V.I.; Eenjin, G. Age of the Khangai batholith and challenge of polychronic batholith formation in Central Asia. *Dokl. Earth Sci.* **2013**, *452*, 1001–1007. [[CrossRef](#)]
26. Yarmolyuk, V.V.; Kozlovsky, A.M.; Travin, A.V.; Kirnozova, T.I.; Fugzan, M.M.; Kozakov, I.K.; Plotkina, Y.V.; Eenzhin, G.; Oyuunchimeg, T.; Sviridova, O.E. Duration of formation and geodynamic nature of the giant batholiths of Central Asia: Data from geological and geochronological studies of the Khangai batholith. *Stratigr. Geol. Correl.* **2019**, *27*, 79–102. [[CrossRef](#)]
27. Kovalenko, V.I.; Yarmolyuk, V.V.; Kovach, V.P.; Kotov, A.B.; Kozakov, I.K.; Salnikova, E.B.; Larin, A.M. Isotope provinces, mechanisms of generation and sources of the continental crust in the Central Asian Mobile Belt: Geological and isotopic evidence. *J. Asian Earth Sci.* **2004**, *23*, 605–627. [[CrossRef](#)]
28. Savatenkov, V.M.; Smirnova, Z.B.; Yarmolyuk, V.V.; Kozlovsky, A.M.; Sviridova, O.E. Nd and Pb isotopic composition of granitoids in the Khangai batholith as an indicator of crust-forming processes in the terranes of the Central Asian orogenic belt. *Petrology* **2018**, *26*, 351–367. [[CrossRef](#)]
29. Yarmolyuk, V.V.; Kozlovsky, A.M.; Savatenkov, V.M.; Kovach, V.P.; Kozakov, I.K.; Kotov, A.B.; Lebedev, V.I.; Eenzhin, G. Composition, sources and geodynamic nature of giant batholiths of Central Asia: According to geochemical and Nd isotopic studies of granitoids of the Khangai zoned magmatic area. *Petrology* **2016**, *24*, 468–498. [[CrossRef](#)]
30. Izokh, A.E.; Polyakov, G.V.; Gibsher, A.S.; Balykin, P.A.; Zhuravlev, D.Z.; Parkhomenko, V.A. High-alumina stratified gabbroids of the Central-Asian fold belt: Geochemistry, Sm-Nd isotopic AGE, and geodynamic conditions of formation. *Russ. Geol. Geophys.* **1998**, *39*, 1565–1577.
31. Sal'nikova, E.B.; Yakovleva, S.Z.; Kotov, A.B.; Tolmacheva, E.V.; Plotkina, Y.V.; Fedoseenko, A.M.; Kozlovskii, A.M.; Yarmolyuk, V.V. Crystallogenes of zircon in alkaline granites and specifics of zircon U-Pb dating: A case study of the Khangai magmatic area. *Petrology* **2014**, *22*, 450–461. [[CrossRef](#)]
32. Shapovalova, M.; Tolstykh, N.; Shelepaev, R.; Kalugin, V. PGE-Cu-Ni Mineralization of Mafic-Ultramafic Massifs of the Khangai Upland, Western Mongolia. *Minerals* **2020**, *10*, 942. [[CrossRef](#)]
33. Kuzmin, M.I.; Yarmolyuk, V.V. Mantle plumes of Central Asia (Northeast Asia) and their role in forming endogenous deposits. *Russ. Geol. Geophys.* **2014**, *55*, 120–143. [[CrossRef](#)]

34. Sengor, A.M.C.; Natalin, B.A.; Burtman, V.S. Evolution of the Altaid Tectonic Collage and Paleozoic Crustal Growth in Eurasia. *Nature* **1993**, *364*, 299–307. [[CrossRef](#)]
35. Xiao, W.J.; Zhang, L.C.; Qin, K.Z.; Sun, S.; Li, J.L. Paleozoic accretionary and collisional tectonics of the Eastern Tianshan (China): Implications for the continental growth of Central Asia. *Am. J. Sci.* **2004**, *304*, 370–395. [[CrossRef](#)]
36. Windley, B.F.; Alexeiev, D.; Xiao, W.J.; Kroner, A.; Badarch, G. Tectonic models for accretion of the Central Asian Orogenic Belt. *J. Geol. Soc.* **2007**, *164*, 31–47. [[CrossRef](#)]
37. Kruk, N.N.; Rudnev, S.N.; Vladimirov, A.G.; Shokalsky, S.P.; Kovach, V.P.; Serov, P.A.; Volkova, N.I. Early-Middle Paleozoic granitoids in Gorny Altai, Russia: Implications for continental crust history and magma sources. *J. Asian Earth Sci.* **2011**, *42*, 928–948. [[CrossRef](#)]
38. Safonova, I.; Seltmann, R.; Kroner, A.; Gladkochub, D.; Schulmann, K.; Xiao, W.J.; Kim, J.; Komiya, T.; Sun, M. A new concept of continental construction in the Central Asian Orogenic Belt (compared to actualistic examples from the Western Pacific). *Episodes* **2011**, *34*, 186–196. [[CrossRef](#)]
39. Kozakov, I.K.; Kotov, A.B.; Kovach, V.P.; Sal'nikova, E.B. Crust-forming processes in the geological development of the Baidarik block of Central Mongolia: Sm-Nd isotope data. *Petrology* **1997**, *5*, 240–248.
40. Badarch, G.; Cunningham, W.D.; Brian, F.W. A new terrane subdivision for Mongolia: Implications for the Phanerozoic crustal growth of central Mongolia. *J. Asian Earth Sci.* **2002**, *21*, 87–110. [[CrossRef](#)]
41. Tomurtogoo, O. Tectonics of Mongolia. In *Tectonics of Northern, Central and Eastern Asia, Explanatory Note to the Tectonic Map of Northern Central Eastern Asia and Adjacent Areas at Scale 1:2500000*; VSEGEI Printing House: Saint Petersburg, Russia, 2014; pp. 110–126.
42. Hamilton, W.B. Form of the Sudbury lopolith. *Can. Miner.* **1960**, *6*, 437–447.
43. Naldrett, A.J. *Magmatic Sulfide Deposits: Geology, Geochemistry and Exploration*, 1st ed.; Springer: Berlin/Heidelberg, Germany, 2004; p. 730.
44. Williams, I.S. U-Th-Pb Geochronology by Ion Microprobe. *Rev. Econ. Geol.* **1998**, *7*, 1–35.
45. Vermeesch, P. Dissimilarity measures in detrital geochronology. *Earth Sci. Rev.* **2018**, *178*, 310–321. [[CrossRef](#)]
46. Karmanova, N.G.; Karmanov, N.S. Universal Method of X-ray Fluorescence Silicate Analysis of Rocks on the ARL-9900XP Spectrometer. In Proceedings of the All-Russian Conference on X-ray Spectral Analysis, Novosibirsk, Russia, 19–23 September 2011; p. 126.
47. Nikolaeva, I.V.; Palesskiy, S.V.; Kozmenko, O.A.; Anoshin, G.N. Determination of rare-earth and highly charged elements in standard geological samples by inductively coupled plasma mass spectrometry (ICP-MS). *Geochemistry* **2008**, *10*, 1085–1091.
48. Boynton, W.V. Geochemistry of the rare earth elements: Meteorite studies. In *Rare Earth Element Geochemistry*; Henderson, P., Ed.; Elsevier: New York, NY, USA, 1984; pp. 63–114.
49. McDonough, W.F.; Sun, S.S.; Ringwood, A.E.; Jagoutz, E.; Hofmann, A.W. Potassium, Rubidium and Cesium in the Earth and Moon and the evolution of the mantle of the Earth. *Geochim. Cosmochim. Acta* **1992**, *56*, 1001–1012. [[CrossRef](#)]
50. Tanaka, T.; Amakawa, H.; Togashi, S.; Kamioka, H. JNdi-1: A neodymium isotopic reference in consistency with La Jolla neodymium. *Chem. Geol.* **2000**, *168*, 279–281. [[CrossRef](#)]
51. Weis, D.; Kieffer, B.; Maerschalk, C.; Barling, J.; Jong, J.D.; Williams, G.A.; Hanano, D.; Pretorius, W.; Mattielli, N.; Scoates, J.S.; et al. High-precision isotopic characterization of USGS reference materials by TIMS and MC-ICP-MS Geochem. *Geophys. Geosyst.* **2006**, *7*, 1525–2027. [[CrossRef](#)]
52. Han, L.; Tanweer, A.; Szaran, J.; Halas, S. A modified technique for the preparation of SO<sub>2</sub> from sulphates and sulphides for sulfur isotope analyses. *Isot. Environ. Health Stud.* **2002**, *38*, 177–183. [[CrossRef](#)]
53. Heaman, L.M.; Bowins, R.; Crocket, J. The chemical composition of igneous zircon suites: Implications for geochemical tracer studies. *Geochim. Cosmochim. Acta* **1990**, *54*, 1597–1607. [[CrossRef](#)]
54. Hoskin, P.W.O.; Schaltegger, U. The composition of zircon and igneous and metamorphic petrogenesis. *Rev. Mineral. Geochem.* **2003**, *53*, 25–104. [[CrossRef](#)]
55. Morimoto, N.; Fabries, J.; Ferguson, A.K.; Ginzburg, I.V.; Ross, M.; Seifert, F.A.; Zussman, J.; Aoki, K.; Gottardi, G. Nomenclature of pyroxenes. *Can. Miner.* **1989**, *27*, 143–156. [[CrossRef](#)]
56. Leake, B.E.; Woolley, A.R.; Birch, W.D.; Burke, E.A.J.; Ferraris, G.; Grice, J.D.; Hawthorne, F.C.; Kisch, H.J.; Krivovichev, V.G.; Schumacher, J.C.; et al. Nomenclature of amphiboles: Additions and revisions to the International Mineralogical Association's amphibole nomenclature. *Can. Miner.* **2003**, *41*, 1355–1370. [[CrossRef](#)]
57. Irvine, T.N.; Baragar, W.R.A. A guide to the chemical classification of the common volcanic rocks. *Can. J. Earth Sci.* **1971**, *8*, 523–548. [[CrossRef](#)]
58. Chaussidon, M.; Lorand, J.-P. Sulphur isotope composition of orogenic spinel lherzolite massifs from Ariege (North-Eastern Pyrenees, France): An ion microprobe study. *Geochim. Cosmochim. Acta* **1990**, *54*, 2835–2846. [[CrossRef](#)]
59. Zhao, Y.; Xue, C.; Zhao, X.; Yang, Y.; Ke, J.; Zu, B. Variable mineralization processes during the formation of the Permian Hulu Ni-Cu sulfide deposit, Xinjiang, Northwestern China. *J. Asian Earth Sci.* **2016**, *126*, 1–13. [[CrossRef](#)]
60. Zindler, A.; Hart, S.R. Chemical geodynamics. *Ann. Rev. Earth Planet. Sci.* **1986**, *14*, 493–571. [[CrossRef](#)]
61. Zhang, Y.-L.; Liu, C.-Z.; Ge, W.-C.; Wu, F.-Y.; Chu, Z.-Y. Ancient sub-continental lithospheric mantle (SCLM) beneath the eastern part of the Central Asian Orogenic Belt (CAOB): Implications for crust-mantle decoupling. *Lithos* **2011**, *126*, 233–247. [[CrossRef](#)]

62. Khosbayar, P.; Byamba, B.; Binderya, T.; Gansukh, Z.; Enkhuvshin, K.; Bataa, C.; Gaechimeg, Y.; Erdenechimeg, J. *Geological Map, Ugiinuur Region L-48-I, II, Scale: 1:200000. Central Geological Expedition of MG and GRP MPR*; Mineral Resources Authority of Mongolia—Geological Office: Ulaanbaatar, Mongolia, 1987.
63. Izokh, A.E.; Polyakov, G.V.; Krivenko, A.P.; Bognibov, V.I.; Bayarbileg, L. *The Gabbro Formation of Western Mongolia*, 1st ed.; Nauka: Novosibirsk, Russia, 1990; p. 269.
64. Izokh, A.E.; Mayorova, O.N.; Lavrentiev, Y.G. Minerals of the platinum metals in the Nomgon troctolite–anorthozite–gabbro intrusive massif (Mongolia). *Russ. Geol. Geophys.* **1992**, *33*, 104–110.
65. Gavrilova, S.P.; Luchitskaya, A.I.; Frikh-Khar, D.I.; Orolmaa, D.; Badamgarav, J. *Volcano-Plutonic Associations of Central Mongolia*, 1st ed.; Nauka: Moscow, Russia, 1991; p. 229.
66. Yarmolyuk, V.V.; Kovalenko, V.I.; Kozakov, I.K.; Sal'nikova, E.B.; Bibikova, E.V.; Kovach, V.P.; Kozlovsky, A.M.; Kotov, A.B.; Lebedev, V.I.; Eenjin, G.; et al. The age of the Khangai batholith and the problem of batholith formation in Central Asia. *Dokl. Earth Sci.* **2008**, *423*, 1223–1228. [[CrossRef](#)]
67. Izokh, A.E.; Vishnevskii, A.V.; Polyakov, G.V.; Kalugin, V.M.; Shelepaev, R.A.; Egorova, V.V.; Oyunchimeg, T. The ureg nuur Pt-bearing volcanoplutonic picrate-basalt association in the Mongolian Altay as evidence for a cambrian-ordovician Large Igneous province. *Russ. Geol. Geophys.* **2010**, *51*, 521–533. [[CrossRef](#)]
68. Wager, L.R.; Brown, G.M. *Layered Igneous Rocks*; W.H. Freeman: San Francisco, CA, USA, 1967; p. 588.
69. Kislov, E.V. *The Ioko-Dovyren Layered Massif*, 2nd ed.; RAS SD Buryat Scientific Centre Publishing House: Ulan-Ude, Russia, 1998; p. 264.
70. Izokh, A.E.; Polyakov, G.V.; Hoa, T.T.; Balykin, P.A.; Phuong, N.T. Permian-triassic ultramafic-mafic magmatism of Northern Vietnam and Southern China as expression of plume magmatism. *Russ. Geol. Geophys.* **2005**, *46*, 922–932.
71. Kuz'min, V.K.; Tuganova, E.V. New data on the isotope composition of sulfur in the copper-nickel sulfide ores of the northwestern part of the Siberian Platform. *Sov. Geol. Geophys.* **1977**, *18*, 98–100.
72. Malitch, K.; Latypov, R.; Badanina, I.; Sluzhenikin, S. Insights into ore genesis of Ni-Cu-PGE sulfide deposits of the Noril'sk Province (Russia): Evidence from copper and sulfur isotopes. *Lithos* **2014**, *204*, 172–187. [[CrossRef](#)]
73. Arndt, N.T.; Czamanske, G.K.; Walker, R.J.; Chauvel, C.; Fedorenko, V.A. Geochemistry and origin of the intrusive hosts of the Noril'sk-Talnakh Cu-Ni-PGE sulfide deposits. *Econ. Geol.* **2003**, *98*, 495–515. [[CrossRef](#)]
74. Li, C.; Ripley, E.M.; Naldrett, A.J. Compositional variations of olivine and sulfur isotopes in the Noril'sk and Talnakh intrusions, Siberia: Implications for ore forming processes in dynamic magma conduits. *Econ. Geol.* **2003**, *98*, 69–86. [[CrossRef](#)]
75. Anders, E.; Grevesse, N. Abundances of the elements: Meteoric and solar. *Geochim. Cosmochim. Acta* **1989**, *53*, 197–214. [[CrossRef](#)]
76. Gao, J.F.; Zhou, M.F.; Lightfoot, P.C.; Wang, C.Y.; Qi, L. Origin of PGE-poor and Cu-rich magmatic sulfides from the Kalatongke deposit, Xinjiang, Northwest China. *Econ. Geol.* **2012**, *107*, 481–506. [[CrossRef](#)]
77. Barnes, S.-J.; Lightfoot, P. Formation of Magmatic Nickel-Sulfide Deposits and Processes Affecting Their Copper and Platinum-Group Element Contents. In *Economic Geology*; Hedenquist, J., Thompson, J., Goldfarb, R., Richards, J., Eds.; Society of Economic Geology: Littleton, MA, USA, 2005; pp. 179–213.
78. Barnes, S.J.; Maier, W.D. The fractionation of Ni, Cu and the noble metals in silicate and sulfide liquids. *Geosci. Canada* **1999**, *13*, 69–106.
79. Song, X.Y.; Wang, Y.S.; Chen, L.M. Magmatic Ni–Cu–(PGE) deposits in magma plumbing systems: Features, formation and exploration. *Geosci. Front.* **2011**, *2*, 375–384. [[CrossRef](#)]

**Disclaimer/Publisher's Note:** The statements, opinions and data contained in all publications are solely those of the individual author(s) and contributor(s) and not of MDPI and/or the editor(s). MDPI and/or the editor(s) disclaim responsibility for any injury to people or property resulting from any ideas, methods, instructions or products referred to in the content.